

Electronic supporting information

Fluorination of mechanochemically synthesized metal-organic frameworks for PFAS adsorption in water

Danilo Marchetti,^{a,b} Enrico Dalcanale,^a Roberta Pinalli,^a Mauro Gemmi,^b Alessandro Pedrini,^{*a} Chiara Massera^{a*}

^aDepartment of Chemistry, Life Sciences and Environmental Sustainability, INSTM UdR Parma, University of Parma, Parco Area delle Scienze 17/A, 43124, Parma, Italy.

^bCenter for Materials Interfaces, Electron Crystallography, Istituto Italiano di Tecnologia, Viale Rinaldo Piaggio 34, 56025 Pontedera, Italy.

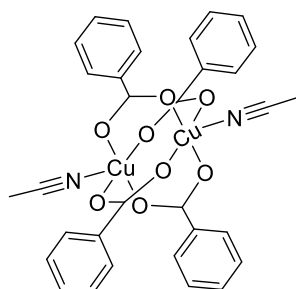
* E-mail: alessandro.pedrini@unipr.it, chiara.massera@unipr.it

Table of contents

1	Synthetic Procedures	S2
1.1	[Cu ₂ (PhCO ₂) ₄ (ACN) ₂] Synthesis	S2
1.2	[Cu ₂ (<i>p</i> -FPhCO ₂) ₄ (ACN) ₂] Synthesis	S2
1.3	TPPM Synthesis	S3
1.4	TPPM-mCPW(<i>p</i> -FPh) Syntheses.....	S3
1.4.1	Mechanochemical	S3
1.4.2	Solvothermal.....	S3
1.5	TPPM-mCPW(Ph) Syntheses	S4
1.5.1	Mechanochemical	S4
1.5.2	Solvothermal.....	S4
1.6	TPPM-CPW(Ph) Syntheses.....	S5
2	Structural Characterization	S6
2.1	Single Crystal X-ray Diffraction (SC-XRD).....	S6
3	Powder X-ray Diffraction (PXRD)	S7
4	3D Electron Diffraction (3D ED) and TEM analysis	S16
5	Thermogravimetric Analyses (TGA)	S23
6	PFAS adsorption experiments	S24
6.1	MOF digestion.....	S24
6.1.1	Sample preparation for ¹⁹ F NMR analysis.....	S24
6.1.2	PFAS exposure experiment	S24
6.2	Uptake of NaPFO using TPPM-mCPW(<i>p</i> -FPh) from aqueous solution	S28
7	DLS Measurement	S30
8	Computational Studies	S31
9	References	S33

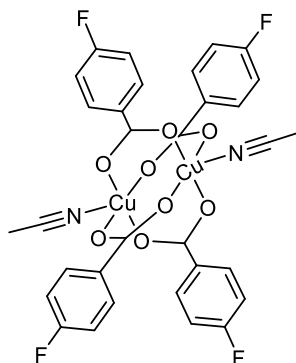
1 Synthetic Procedures

1.1 $[\text{Cu}_2(\text{PhCO}_2)_4(\text{ACN})_2]$ Synthesis



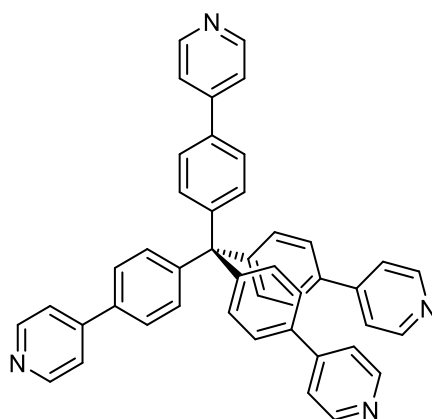
The synthesis was conducted following the procedure reported in the literature.¹

1.2 $[\text{Cu}_2(p\text{-FPhCO}_2)_4(\text{ACN})_2]$ Synthesis



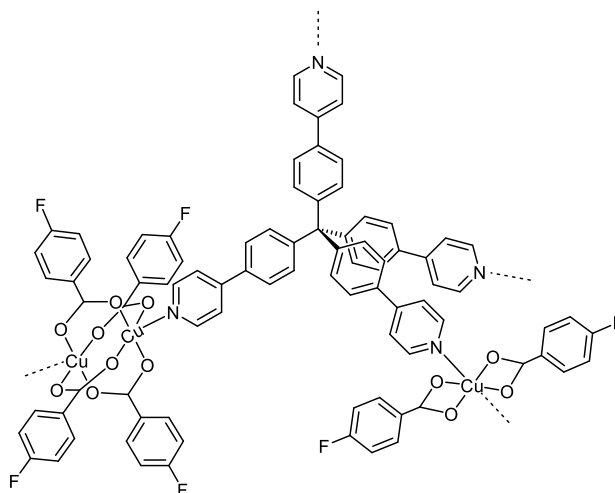
The synthesis was conducted by mixing into an agate mortar 4-fluoro benzoic acid (500 mg, 3.6 mmol) and sodium hydroxide (144 mg, 3.6 mmol). Then, 500 μL of water were added and a liquid assisted grinding (LAG) was performed for 10 minutes. In the meantime, copper sulphate pentahydrate (445 mg, 1.8 mmol) was added to 5 mL of water and sonicated for 20 minutes until complete solubilization. The mechanochemical product was then solubilized in 10 mL of water. The copper sulphate solution was then carefully added to the sodium benzoate solution, to immediately obtain a blue precipitate. The mixture was then cooled into an ice bath and the precipitate filtered off. The obtained solid was subsequently dried and solubilized in 200 mL of acetonitrile (ACN) and molecular sieves (3 \AA) were added to the mixture. After 2h, the reaction mixture was filtered, and the solvent evaporated under reduced pressure. The product was then recrystallized at 4 $^\circ\text{C}$, isolating blue crystals suitable for single crystal X-ray diffraction (Table S1, Figure S1). The solid-state analysis confirmed the structure of the paddle-wheel with two ACN crystallization molecules, leading to a general formula $[\text{Cu}_2(p\text{-FPhCO}_2)_4(\text{ACN})_2] \cdot 2\text{ACN}$ (407 mg, 52% yield).

1.3 TPPM Synthesis



The TPPM synthesis was carried out following the procedure in the literature.^{2,3}

1.4 TPPM-mCPW(*p*-FPh) Syntheses



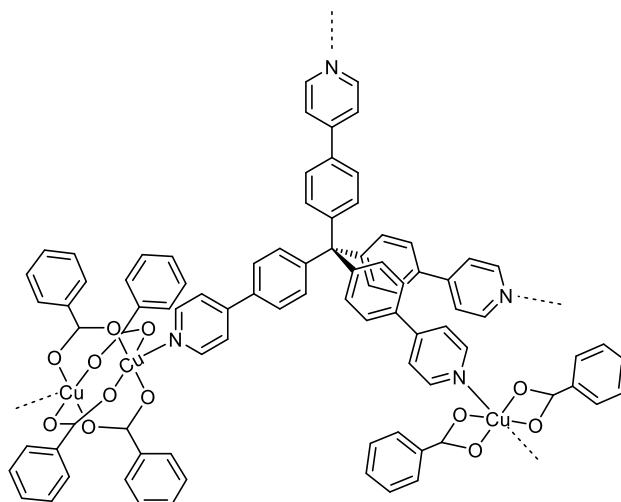
1.4.1 Mechanochemical

The mechanochemical synthesis of **TPPM-mCPW(*p*-FPh)** was carried out placing the **TPPM** molecule (16.07 mg, 25.56 μmol), *p*-fluoro benzoic acid (***p*-FPhA**, 7.64 mg, 54.5 μmol), **[Cu₂(*p*-FPhCO₂)₄(ACN)₂]**·**ACN (39.30 mg, 46.36 μmol) and 60 μL of 1:1 DMF/BnOH in a stainless steel jar with two 5 mm spheres. The mixture was ground into a Retsch mixer mill MM 400 operating at 30 Hz for 30 min. The as-synthesized grinding product was left to evaporate the remaining traces of LAG additive (Figure S3). The obtained blue powder was then washed with a 9:1 CHCl₃/MeOH solution, dried under reduced pressure and characterised through PXRD analysis (29.5 mg, 69 % yield, Figure S6).**

1.4.2 Solvothermal

The **TPPM-mCPW(*p*-FPh)** synthesis was conducted solubilising the **TPPM** molecule (3.32 mg, 5.28 μmol) in 3.0 mL of a 2:1 CHCl₃/^{*i*}PrOH solution, ***p*-FPhA** (7.82 mg, 55.8 μmol) in 2.5 mL of a 1:1 CHCl₃/^{*i*}PrOH solution, and **[Cu₂(*p*-FPhCO₂)₄(ACN)₂]**·**2ACN (9.62 mg, 11.3 μmol) in 3 mL of a 1:2 CHCl₃/^{*i*}PrOH solution. The **TPPM** solution was then placed into a glass tube with a Teflon screw cap, then the ***p*-FPhA** solution followed by the **[Cu₂(*p*-FPhCO₂)₄(ACN)₂]**·**2ACN were carefully added, to obtain three different layers. The reaction was then heated at 80° C for 2 days. The obtained green powder was then rinsed with a 9:1 CHCl₃/MeOH solution and dried under reduced pressure (2.83 mg, 32 % yield). The product was then characterised through PXRD, HAADF-STEM, 3D ED, and TGA analysis (Figure S7, S15, S17, S19 and S26).****

1.5 TPPM-mCPW(Ph) Syntheses



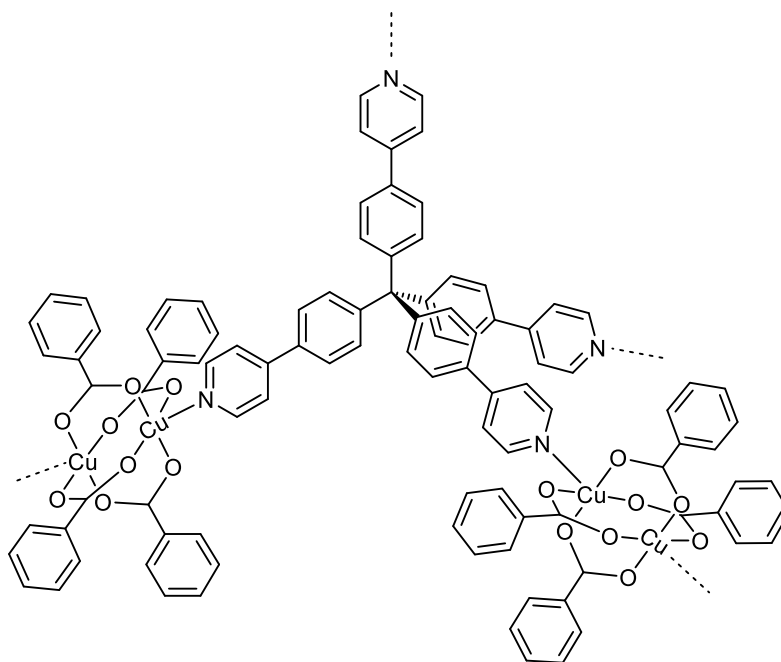
1.5.1 Mechanochemical

The mechanochemical synthesis of **TPPM-mCPW(Ph)** was carried out placing the **TPPM** molecule (16.09 mg, 25.59 μmol), $[\text{Cu}_2(\text{PhCO}_2)_4(\text{ACN})_2]\cdot\text{ACN}$ (38.30 mg, 55.21 μmol) and 60 μL of 2:1 DMF/BnOH in a stainless steel jar with two 5 mm spheres. The mixture was ground into a Retsch mixer mill MM 400 operating at 30 Hz for 30 min. The as-synthesized grinding product was left to evaporate the remaining traces of LAG additive (Figure S9). The obtained blue powder was then washed with a 9:1 $\text{CHCl}_3/\text{MeOH}$ solution, dried under reduced pressure, activated at 180°C for 30 min, and characterised through PXRD analysis (17.6 mg, 44 % yield, Figure S10).

1.5.2 Solvothermal

The **TPPM-mCPW(Ph)** synthesis was carried out adding the **TPPM** molecule (7.10 mg, 11.3 μmol), $[\text{Cu}_2(\text{PhCO}_2)_4(\text{ACN})_2]\cdot\text{ACN}$ (16.08 mg, 21.89 μmol), benzoic acid (153.62 mg, 1.26 mmol), and 10 mL of DMF into a glass tube with a Teflon screw cap. The mixture was then heated up to 90°C for 3 days. The reaction crude was then washed with a 9:1 $\text{CHCl}_3/\text{MeOH}$ solution and dried under reduced pressure (12.7 mg, 72% yield). The product appears as a light-blue powder, which was characterised through PXRD, HAADF-STEM, 3D Ed and TGA analysis (Figure S12, S16, S18, S20 and S27).

1.6 TPPM-CPW(Ph) Syntheses



TPPM-CPW(Ph) was synthesised through liquid assisted grinding, in its solvated phase with BnOH (**TPPM-CPW(Ph)·BnOH**), following the procedure previously reported in literature.¹

2 Structural Characterization

2.1 Single Crystal X-ray Diffraction (SC-XRD)

The crystal structures of $[\text{Cu}_2(p\text{-FPhCO}_2)_4(\text{ACN})_2]\cdot 2\text{ACN}$ at different temperatures were determined by X-ray diffraction on single crystals. Crystal data and experimental details for data collection and structure refinement are reported in Table S1. Intensity data and cell parameters were recorded at 200(2) on a Bruker D8 Venture PhotonII diffractometer (Mo K α radiation $\lambda = 0.71073 \text{ \AA}$). The raw frame data were processed using SAINT and SADABS to yield the reflection data files.⁴ The structures were solved by Direct Methods using the SHELXT program⁵ and refined on F_o^2 by full-matrix least-squares procedures, using SHELXL-2018⁶ in the Olex2-1.5 suite.⁷ All non-hydrogen atoms were refined with anisotropic atomic displacements, except for the disordered solvent molecules. The hydrogen atoms were included in the refinement at idealised geometry and refined “riding” on the corresponding parent atoms. The weighting scheme used in the last cycle of refinement was $w = 1/[\sigma^2 F_o^2 + (0.0826P)^2 + 0.4931P]$, where $P = (F_o^2 + 2F_c^2)/3$. The crystallographic data have been deposited with the Cambridge Crystallographic Data Centre as supplementary publication no. 2440128 and can be obtained free of charge on application to the CCDC, 12 Union Road, Cambridge, CB2 1EZ, UK (e-mail deposit@ccdc.cam.ac.uk or <http://www.ccdc.cam.ac.uk>).

Table S1: Crystallographic information for $[\text{Cu}_2(p\text{-FPhCO}_2)_4(\text{ACN})_2]\cdot 2\text{ACN}$.

Empirical formula	C ₃₆ H ₂₈ Cu ₂ F ₄ N ₄ O ₈
Formula weight	847.70
Temperature/K	200.15
Crystal system	Triclinic
Space group	<i>P</i> -1
<i>a</i> /Å	10.1124(4)
<i>b</i> /Å	10.3357(4)
<i>c</i> /Å	10.4275(4)
α /°	71.530(4)
β /°	70.551(4)
γ /°	67.444(4)
Volume/Å ³	926.42(7)
<i>Z</i>	1
$\rho_{\text{calc}}/\text{cm}^3$	1.519
μ/mm^{-1}	1.224
<i>F</i> (000)	430.0
Radiation	Mo K α ($\lambda = 0.71073$)
2 θ range for data collection/°	4.494 to 61.014
Index ranges	$-14 \leq h \leq 14, -14 \leq k \leq 14, -14 \leq l \leq 14$
Reflections collected	39860
Independent reflections	5631 [$R_{\text{int}} = 0.0644, R_{\text{sigma}} = 0.0295$]
Data/restraints/parameters	5631/16/238
Goodness-of-fit on F^2	1.082
Final <i>R</i> indexes [$I \geq 2\sigma(I)$] ^a	$R_1 = 0.0496, wR_2 = 0.1381$
Final <i>R</i> indexes [all data] ^a	$R_1 = 0.0518, wR_2 = 0.1401$

^a $R_1 = \sum \|F_o\| - \|F_c\| / \sum \|F_o\|, wR_2 = [\sum [w(F_o^2 - F_c^2)^2] / \sum [w(F_o^2)^2]]^{1/2}$

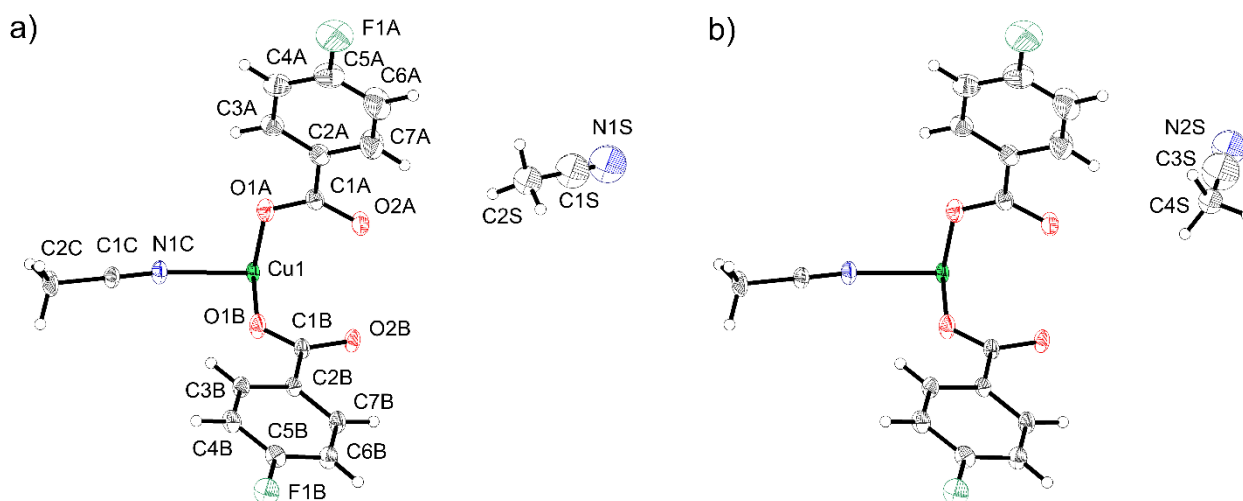


Figure S1: Ortep view of the asymmetric unit of $[\text{Cu}_2(p\text{-FPhCO}_2)_4(\text{ACN})_2]\cdot 2\text{ACN}$ (probability level 30%). The ACN molecule is disordered along two different positions with occupancy of 0.6 (a) and 0.4 (b), respectively.

3 Powder X-ray Diffraction (PXRD)

The powder X-ray diffraction data used for refinement analysis were collected in 0.3 mm borosilicate glass capillary, using Cu $K\alpha_1$ radiation ($\lambda=1.5406 \text{ \AA}$) on a STOE Stadi P equipped with a Ge (111) Johansson focussing monochromator from STOE & Cie and a Mythen2 1K detector from Dectris. Data were preliminarily processed with WinXPOW (by STOE & Cie). The Le Bail refinement on powder X-ray diffraction data was conducted with Jana2020.⁸ Manually selected points were used to describe the background, single crystal data (3D ED) were used to define the unit cell, and cyclic refinements on the entire dataset were used to generate the profile parameters. The peak profile was modelled as a pseudo-Voigt function, corrected due to axial divergence asymmetry and cut outside $20\cdot\text{FMWH}$ range.

The structure solution and Rietveld refinement of *cp*-TPPM-mCPW(*p*-FPh) on PXRD data was conducted with TOPAS-Academic V6.⁹ The angular range of the diffraction data was comprised in the 2θ range of $3\text{-}88^\circ$, the background fitted as Chebyshev polynomial and the peak profile modelled as pseudo-Voigt function, corrected with axial divergence asymmetry. The asymmetric unit was refined using a rigid body with degree of freedom defined through a Z-matrix formalism. The crystallographic data have been deposited with the Cambridge Crystallographic Data Centre as supplementary publication no. 2440131 and can be obtained free of charge on application to the CCDC, 12 Union Road, Cambridge, CB2 1EZ, UK (e-mail deposit@ccdc.cam.ac.uk or <http://www.ccdc.cam.ac.uk>).

Temperature-resolved *in situ* data collections were performed using a High Temperature Attachment for capillaries provided by STOE, collecting each diffraction pattern in a 2θ range of $4\text{-}22^\circ$ every 10°C with a heating ramp of $10^\circ\text{C}/\text{min}$.

The PXRD patterns of the remaining samples were collected using Ni-filtered Cu $K\alpha$ radiation ($\lambda_{K\alpha 1} = 1.5406 \text{ \AA}$, $\lambda_{K\alpha 2} = 1.5444 \text{ \AA}$), on a Rigaku SmartLab XE diffractometer equipped with a HyPix-3000 detector. The data were collected in Bragg-Brentano geometry and processed with SmartLab Studio II (by Rigaku).

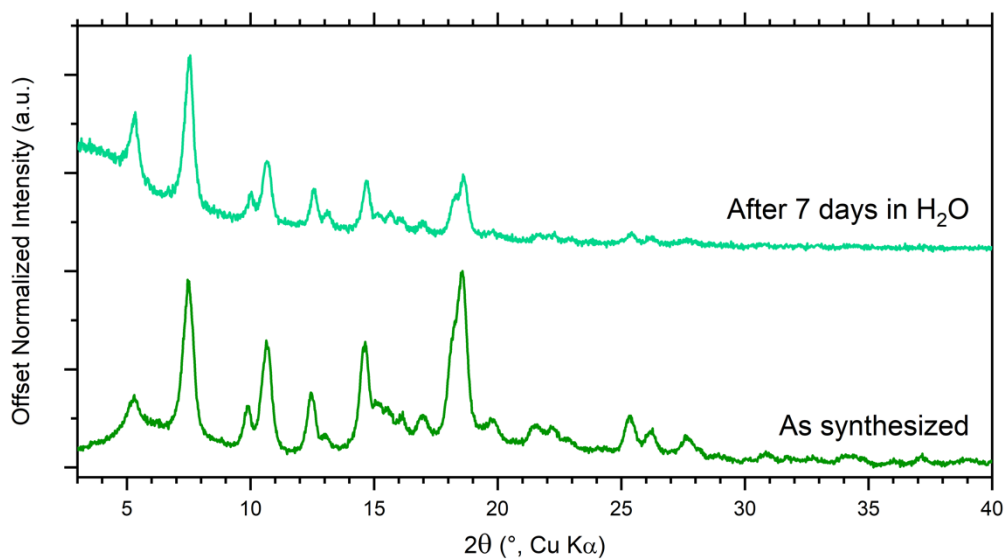


Figure S2: PXRD profile of TPPM-CPW(Ph)·BnOH before and after 7 days of soaking in water.

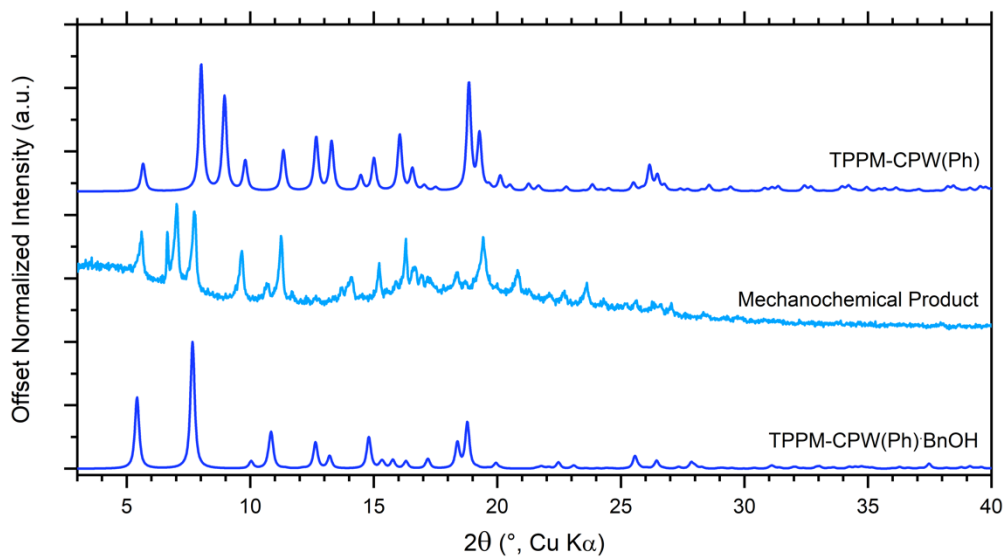


Figure S3: PXRD profile comparison between the mechanochemically synthesized TPPM-mCPW(*p*-FPh), TPPM-CPW(Ph) and TPPM-CPW(Ph)·BnOH.

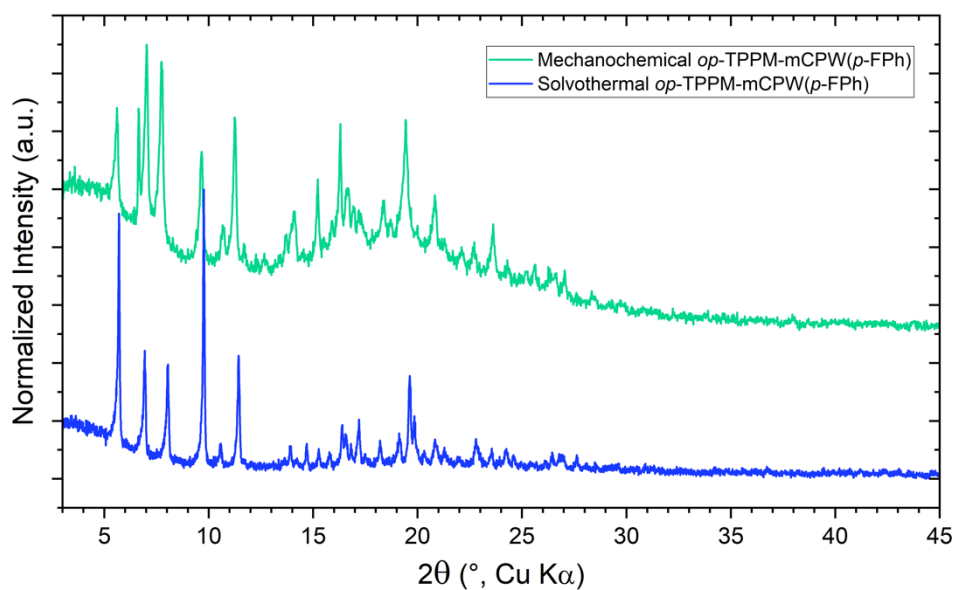


Figure S4: PXRD profile comparison between the mechanochemically and solvothermally synthesized *op*-TPPM-mCPW(*p*-FPh), both before the purification process.

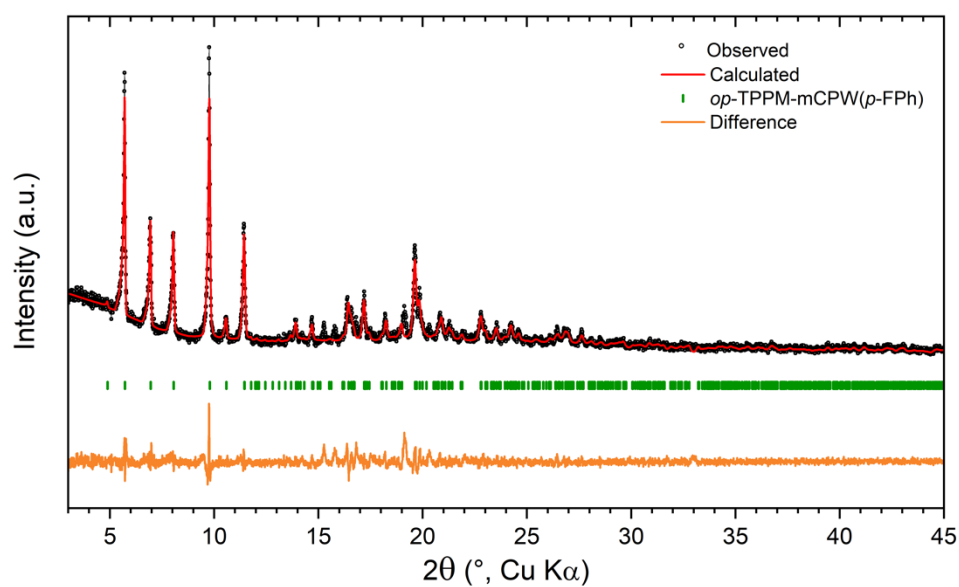


Figure S5: Profile fit from Le Bail refinement on *op*-TPPM-mCPW(*p*-FPh). The refinement converged to $R_p = 2.48\%$, $wR_p = 4.08\%$ and $GOF = 3.72$.

Table S2: Lattice parameter comparison of *op*-TPPM-mCPW(*p*-FPh) MOF between 3D ED and PXRD after Le Bail refinement.

<i>op</i> -TPPM-mCPW(<i>p</i> -FPh)	3D ED	PXRD
$a/\text{\AA}$	25.632(11)	25.0677(10)
$b/\text{\AA}$	7.653(2)	7.6053(4)
$c/\text{\AA}$	23.063(9)	22.7295(8)
$\beta/^\circ$	98.12(3)	99.101(3)
Volume/ \AA^3	4478(3)	4278.8(3)

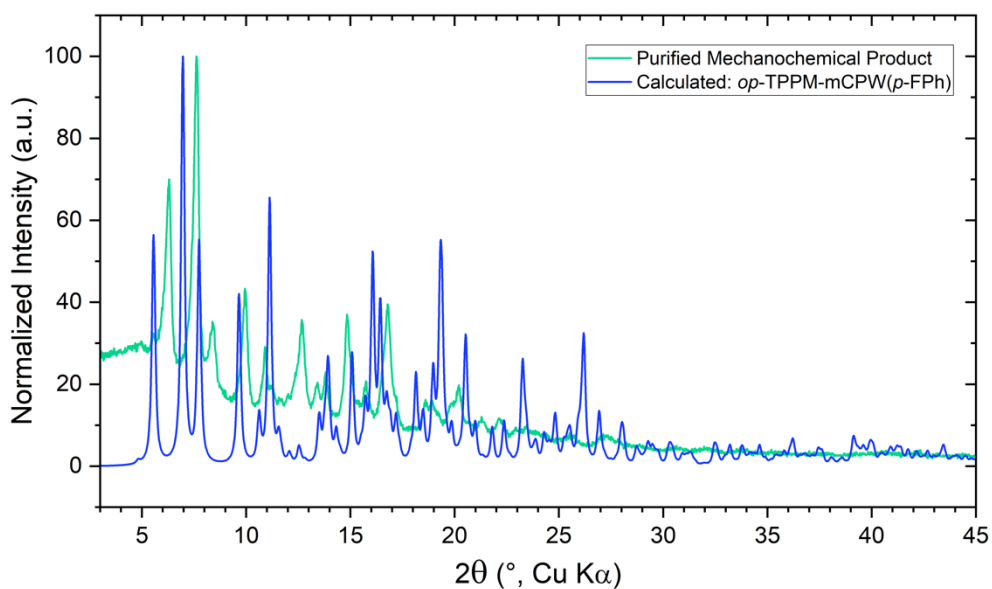


Figure S6: PXRd profile comparison between the purified **TPPM-mCPW(*p*-FPh)** phase and the calculated PXRd pattern of the ***op*-TPPM-mCPW(*p*-FPh)** form. The purification was conducted through a washing process employing a solution of DCM/MeOH 4:1.

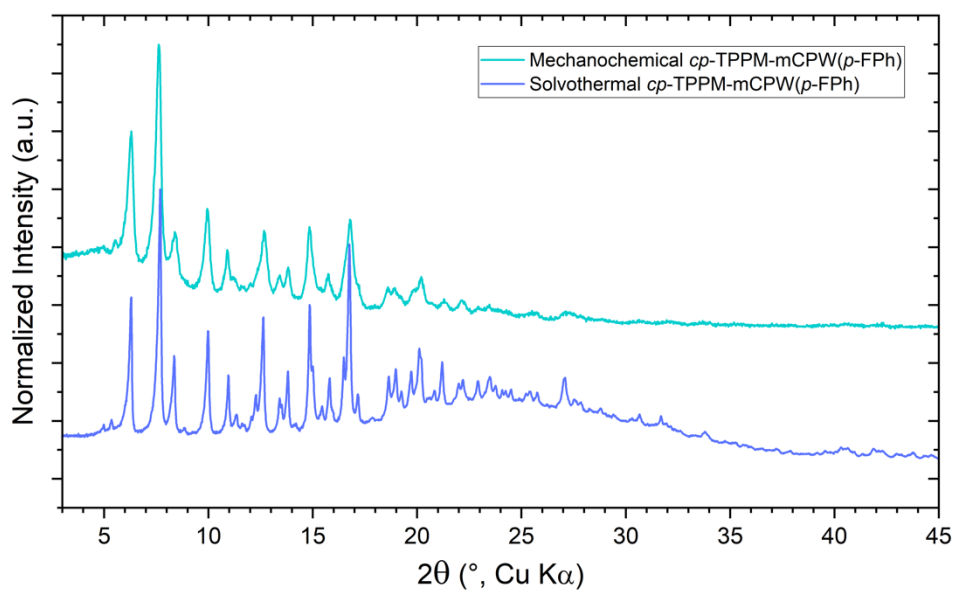


Figure S7: PXRd profile comparison between the mechanochemically and solvothermally synthesized ***cp*-TPPM-mCPW(*p*-FPh)**, both after the purification process.

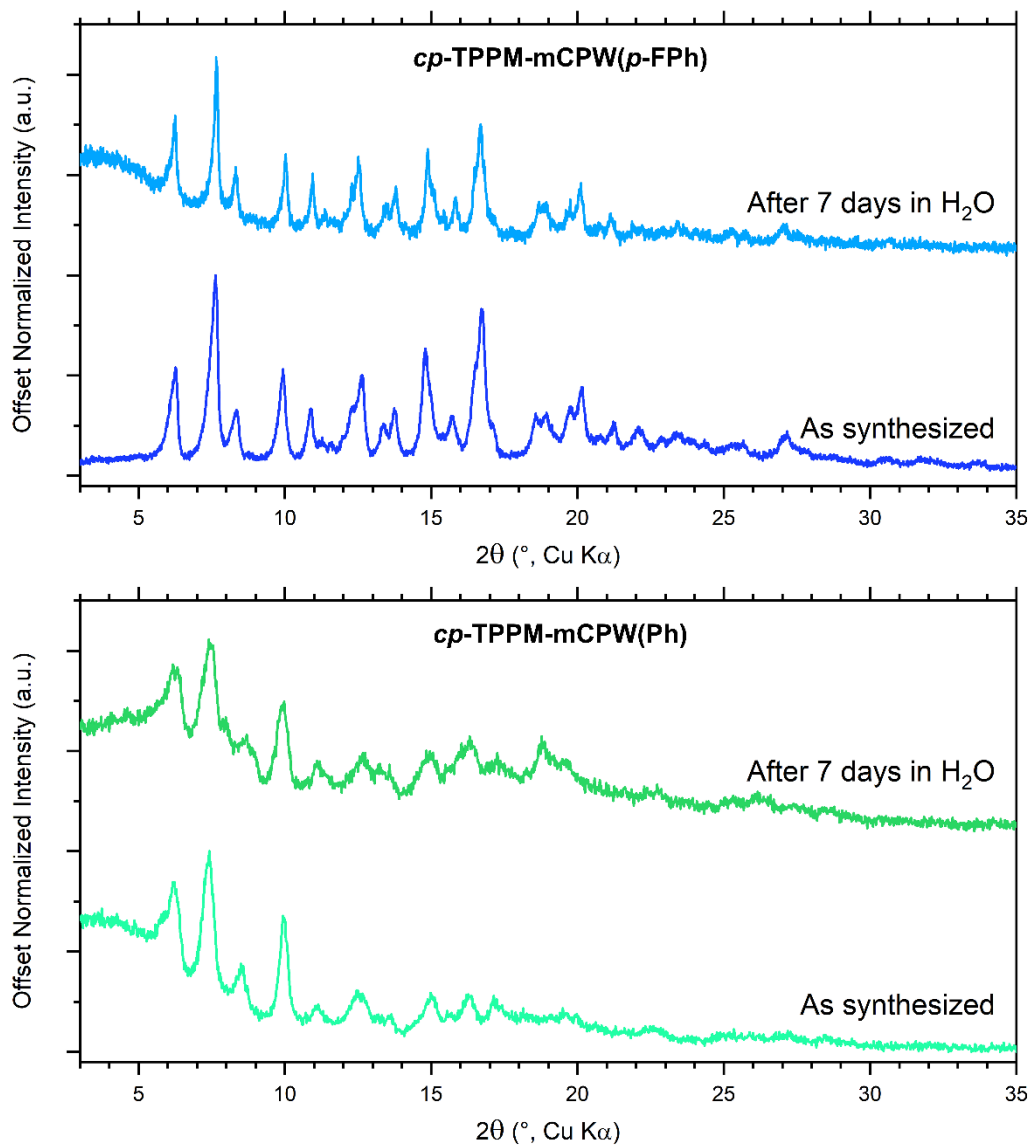


Figure S8: PXRD profile of *cp*-TPPM-mCPW(*p*-FPh) and *cp*-TPPM-mCPW(Ph) before and after 7 days of exposure in water.

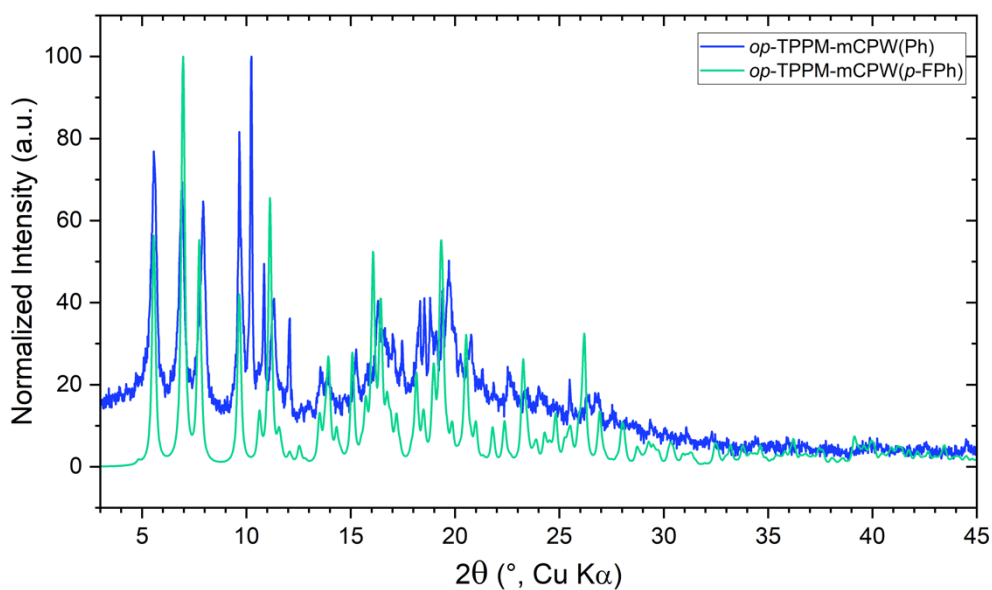


Figure S9: PXR D profile comparison between the mechanochemically synthesized *op*-TPPM-mCPW(Ph) and *op*-TPPM-mCPW(*p*-FPh) calculated from its crystal structure.

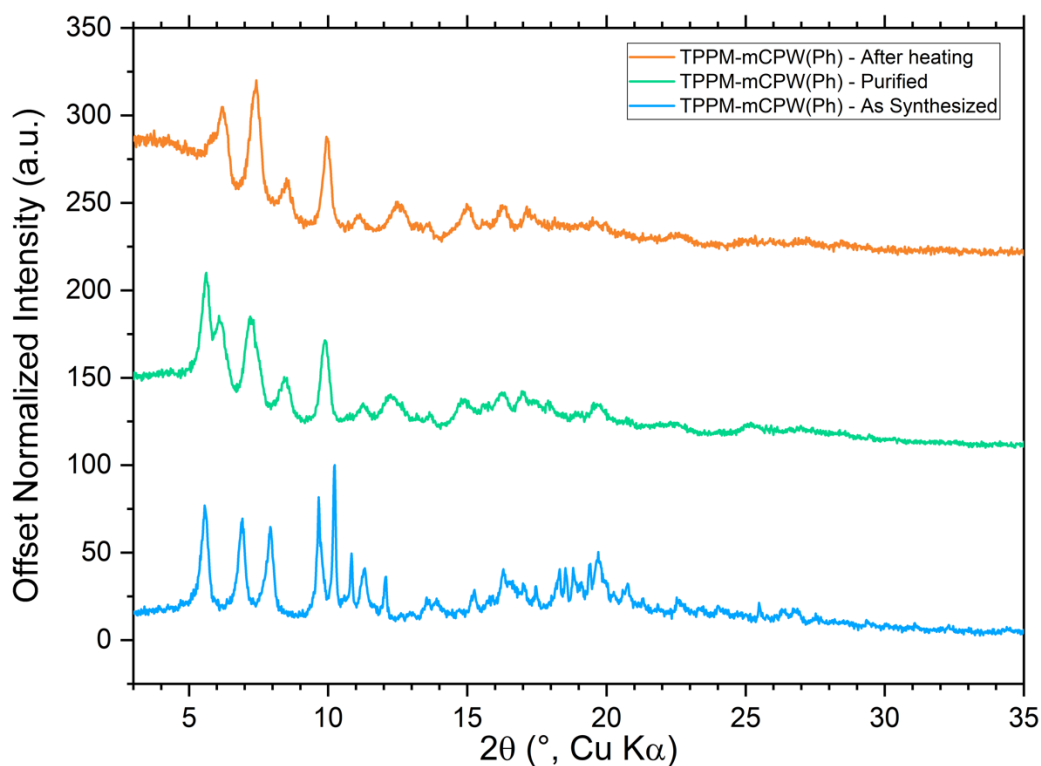


Figure S10: PXR D profile comparison between the mechanochemically synthesized TPPM-mCPW(Ph) as-synthesized and after its purification process, followed by the PXR D profile after the heating treatment at 180 $^{\circ}$ C for 30 min. This figure highlights the phase transition of TPPM-mCPW(Ph) starting from the *op*-TPPM-mCPW(Ph) phase to the *cp*-TPPM-mCPW(Ph) phase.

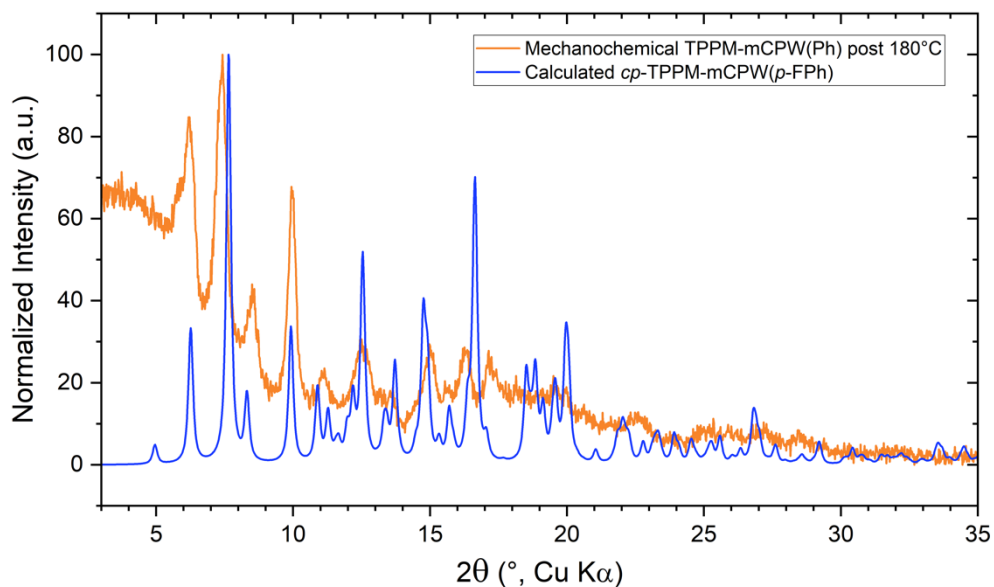


Figure S11: PXRD profile comparison between the mechanochemically synthesized and thermally treated **TPPM-mCPW(Ph)** and the calculated pattern of *cp*-TPPM-mCPW(*p*-FPh).

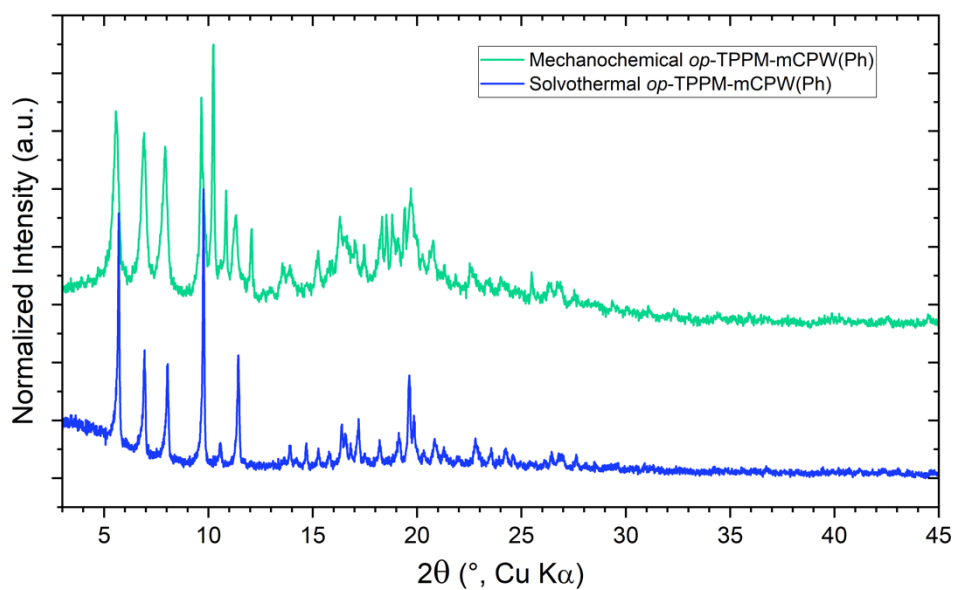


Figure S12: PXRD profile comparison between the mechanochemically and solvothermally synthesized *op*-TPPM-mCPW(Ph), respectively as-synthesized and after the purification process.

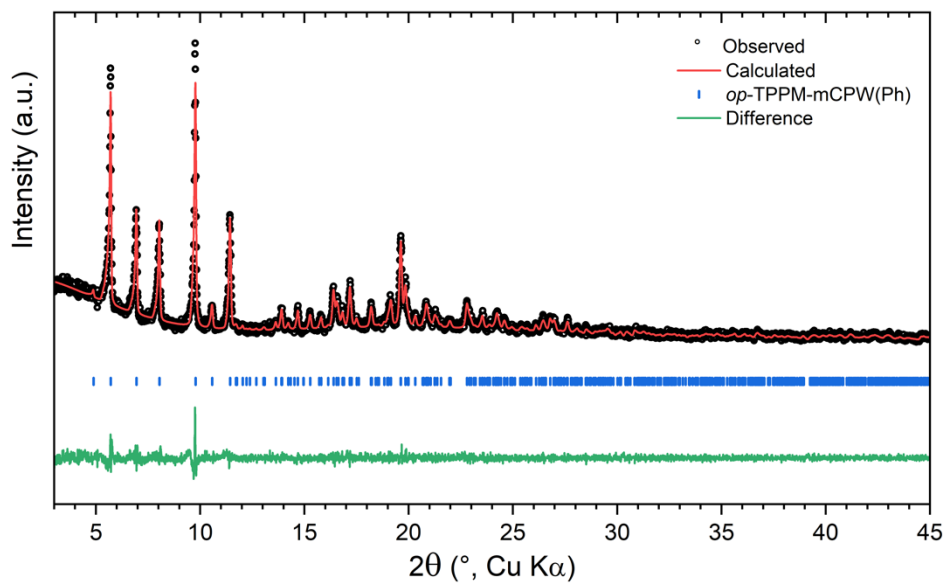


Figure S13: Profile fit from Le Bail refinement on *op*-TPPM-mCPW(Ph). The refinement converged to $R_p = 6.85\%$, $wR_p = 8.69\%$ and $GOF = 6.37$.

Table S3: Lattice parameter comparison of *op*-TPPM-mCPW(Ph) MOF between 3D ED and PXRD after LeBail refinement.

<i>op</i> -TPPM-mCPW(Ph)	3D ED	PXRD
$a/\text{\AA}$	25.534(7)	25.743(2)
$b/\text{\AA}$	7.485(3)	7.5507(8)
$c/\text{\AA}$	22.287(9)	22.229(2)
$\beta/^\circ$	98.81(3)	99.039(4)
Volume/ \AA^3	4209.3(3)	4266.4(5)

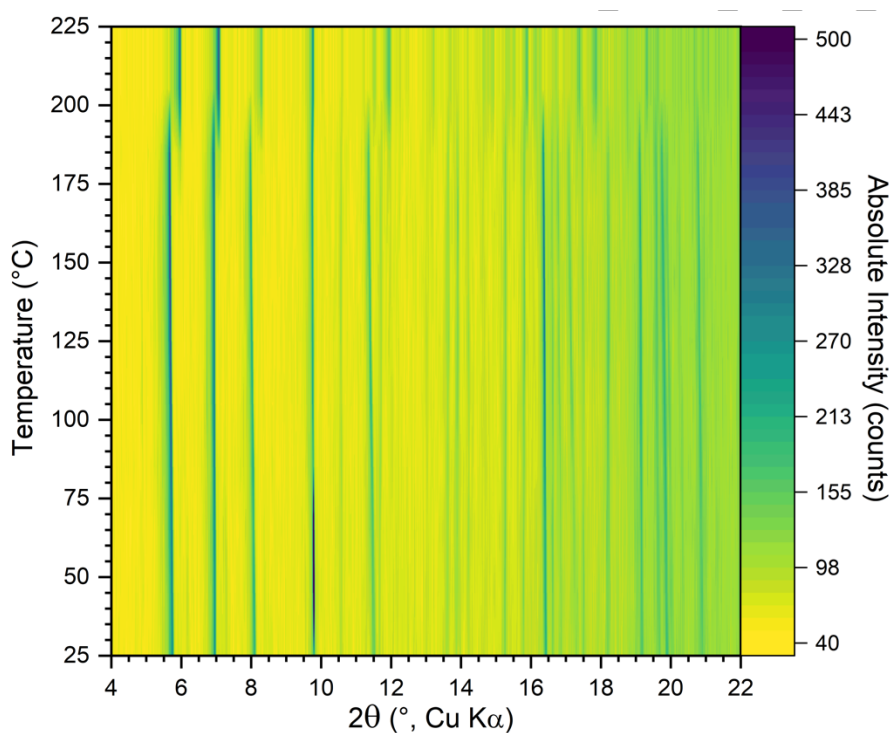


Figure S14: Temperature-induced phase transition of **TPPM-mCPW(Ph)** conducted on the as-synthesized product to induce its conversion from *op* to *cp* form. The analysis was monitored by temperature-resolved in situ powder X-ray diffraction; 2D projection along the intensity axis.

Table S4: Crystallographic information for *cp*-TPPM-mCPW(*p*-FPh).

Empirical formula	C ₈₇ H ₅₆ Cu ₃ F ₆ N ₄ O ₁₂
Formula weight	1654.01
Temperature/K	298
Crystal system	Monoclinic
Space group	<i>P2/n</i>
<i>a</i> /Å	21.84(5)
<i>b</i> /Å	8.117(18)
<i>c</i> /Å	23.74(5)
α /°	90
β /°	103.302(8)
γ /°	90
Volume/Å ³	4096(16)
<i>Z</i>	2
ρ_{calc} /cm ³	1.3435(3)
Radiation	CuK α ($\lambda = 1.5406$ Å)
2θ range for data collection/°	3.0 to 79.995
Index ranges	$0 \leq h \leq 18, 0 \leq k \leq 6, -19 \leq l \leq 19$
Reflections collected	2529
Goodness-of-fit on F^2	2.897
Final R_p indexes	$R_1 = 0.0285, wR_2 = 0.0403$

$$^a R_p = \frac{\sum ||I_o| - |I_c||}{\sum |I_o|}, wR_p = \left[\frac{\sum [w(I_o^2 - I_c^2)^2]}{\sum [w(I_o^2)^2]} \right]^{1/2}$$

4 3D Electron Diffraction (3D ED) and TEM analysis

Scanning transmission electron microscopy imaging and 3D electron diffraction were carried out on a Zeiss Libra 120 transmission electron microscope, equipped with a LaB₆ thermionic source operating at 120 kV ($\lambda=0.0335$ Å) and a Timepix single-electron detector by ASI for collecting diffraction patterns in low dose mode. 3D electron diffraction data were collected on single nanocrystals in nanodiffraction mode with a parallel electron beam of 150 nm in diameter. Imaging was carried out in STEM mode with a high angular dark field detector (HAADF). During the STEM-cRED data collection protocol, the diffracted electrons pass through the high-angle annular dark field (HAADF) STEM detector allowing the live-tracking of the crystal.^{10,11} In the meantime, the Timepix single electron detector, placed below the HAADF, is collecting the electron diffraction patterns. The 3D ED data were analysed using the software PETS.¹² The ab-initio structure determination of *op*-TPPM-mCPW(*p*-FPh) was performed using SHELXT,⁵ while for *op*-TPPM-mCPW(Ph) was employed the Superflip¹³ package. Data were refined with a fully kinematical approximation, *i.e.* neglecting dynamical scattering and assuming that I_{hkl} is proportional to $|F_{hkl}|^2$. Least-squares structure refinement was performed with the software SHELXL-2014⁶ interfaced with Olex2-1.5.⁷ The crystallographic data have been deposited with the Cambridge Crystallographic Data Centre as supplementary publications no. 2440129- 2440130 and can be obtained free of charge on application to the CCDC, 12 Union Road, Cambridge, CB2 1EZ, UK (e-mail deposit@ccdc.cam.ac.uk or <http://www.ccdc.cam.ac.uk>).

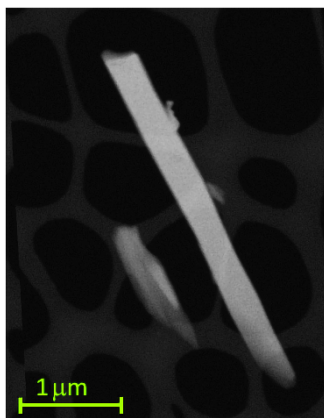


Figure S15: HAADF-STEM image of the *op*-TPPM-mCPW(*p*-FPh) nanocrystals used for the 3D ED data collection.

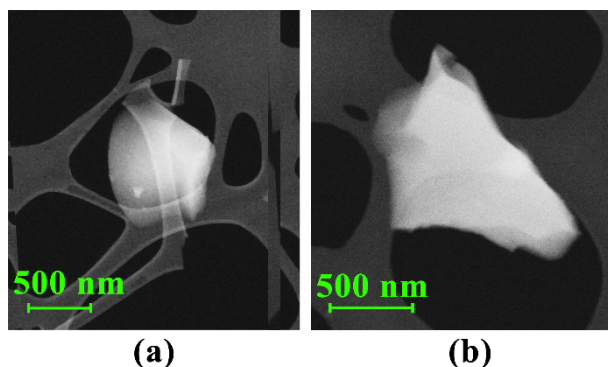


Figure S16: HAADF-STEM image of the *op*-TPPM-mCPW(Ph) nanocrystals used for the 3D ED data collection.

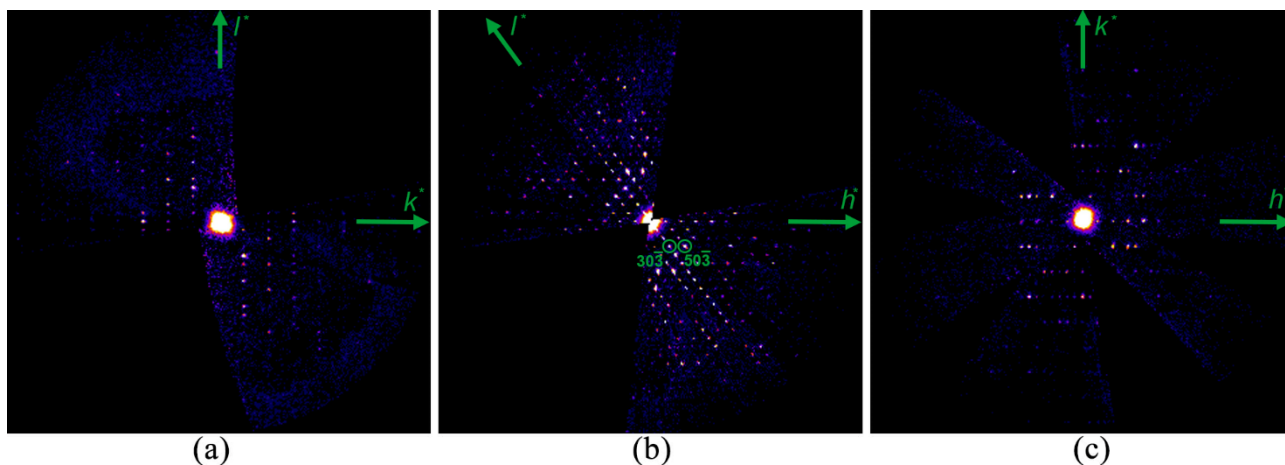


Figure S17: Reciprocal space section of *op*-TPPM-mCPW(*p*-FPh) reconstructed with PETS2 from the 3D ED data collection: (a) $0kl$, (b) $h0l$, (c) $hk0$. The $h0l$ reciprocal plane section shows the extinction rule $h + l = 2n$.

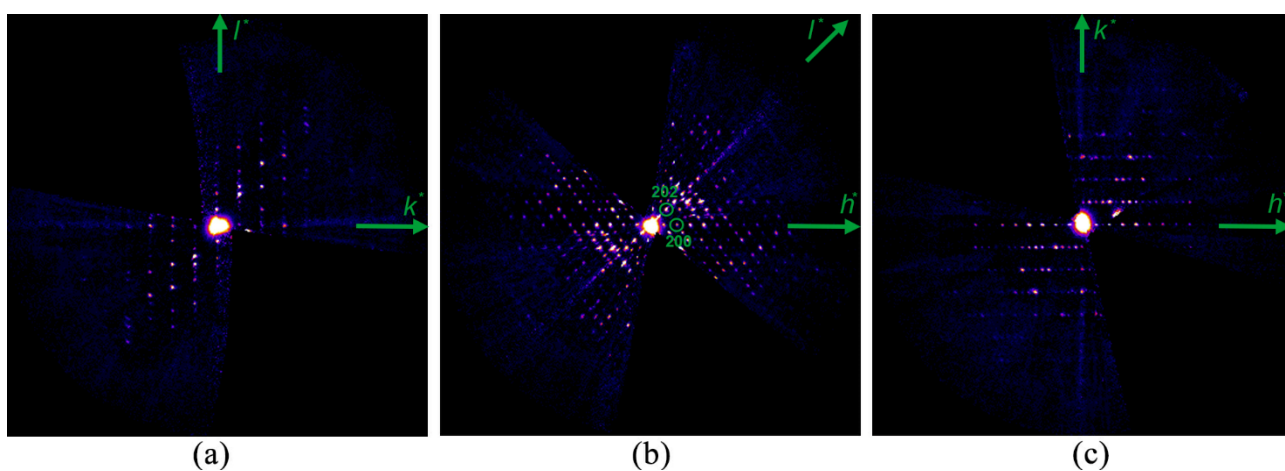


Figure S18: Reciprocal space section of *op*-TPPM-mCPW(Ph) reconstructed with PETS2 from the 3D ED data collection: (a) $0kl$, (b) $h0l$, (c) $hk0$. The $h0l$ reciprocal plane section shows the extinction rule $h + l = 2n$.

Table S5: Crystallographic information for *op*-TPPM-mCPW(*p*-FPh).

Empirical formula	C _{97.5} H _{63.5} Cu ₃ F _{7.5} N ₄ O ₁₅
Formula weight	1864.22
Temperature/K	293(2)
Crystal system	monoclinic
Space group	<i>P2/n</i>
<i>a</i> /Å	25.632(11)
<i>b</i> /Å	7.653(2)
<i>c</i> /Å	23.063(9)
α /°	90
β /°	98.12(3)
γ /°	90
Volume/Å ³	4478(3)
<i>Z</i>	2
ρ_{calc} /cm ³	1.382
F(000)	682.0
Radiation	Electrons ($\lambda = 0.0335$ Å)
2 θ range for data collection/°	0.104 to 2.132
Index ranges	-28 ≤ <i>h</i> ≤ 28, -8 ≤ <i>k</i> ≤ 8, -25 ≤ <i>l</i> ≤ 25
Reflections collected	14061
Independent reflections	4472 [<i>R</i> _{int} = 0.3794, <i>R</i> _{sigma} = 0.3337]
Data/restraints/parameters	4472/148/218
Goodness-of-fit on F ²	1.382
Final <i>R</i> indexes [<i>I</i> ≥ 2 σ (<i>I</i>)] ^a	<i>R</i> ₁ = 0.2653, <i>wR</i> ₂ = 0.5388
Final <i>R</i> indexes [all data] ^a	<i>R</i> ₁ = 0.3893, <i>wR</i> ₂ = 0.6123

$$^a R_1 = \frac{\sum \|F_o\| - \|F_c\|}{\sum \|F_o\|}, wR_2 = \left[\frac{\sum [w(F_o^2 - F_c^2)^2]}{\sum [w(F_o^2)^2]} \right]^{1/2}$$

Table S6: Crystallographic information for *op*-TPPM-mCPW(Ph)

Empirical formula	C ₉₀ H ₆₉ Cu ₃ N ₅ O ₁₃
Formula weight	1619.20
Temperature/K	293(2)
Crystal system	Monoclinic
Space group	<i>P2/n</i>
<i>a</i> /Å	25.534(3)
<i>b</i> /Å	7.485(8)
<i>c</i> /Å	22.287(3)
α /°	90
β /°	98.814(10)
γ /°	90
Volume/Å ³	4209.3(8)
<i>Z</i>	2
ρ_{calc} /cm ³	1.278
F(000)	632.0
Radiation	Electrons ($\lambda = 0.0335$ Å)
2 θ range for data collection/°	0.124 to 2.132
Index ranges	-28 ≤ <i>h</i> ≤ 28, -8 ≤ <i>k</i> ≤ 8, -24 ≤ <i>l</i> ≤ 24
Reflections collected	16451
Independent reflections	5739 [<i>R</i> _{int} = 0.3109, <i>R</i> _{sigma} = 0.2602]
Data/restraints/parameters	5739/71/199
Goodness-of-fit on F ²	1.366
Final <i>R</i> indexes [<i>I</i> ≥ 2 σ (<i>I</i>)] ^a	<i>R</i> ₁ = 0.2553, <i>wR</i> ₂ = 0.5452
Final <i>R</i> indexes [all data] ^a	<i>R</i> ₁ = 0.3500, <i>wR</i> ₂ = 0.6063

$$^a R_1 = \frac{\sum \|F_o\| - \|F_c\|}{\sum \|F_o\|}, wR_2 = \left[\frac{\sum [w(F_o^2 - F_c^2)^2]}{\sum [w(F_o^2)^2]} \right]^{1/2}$$

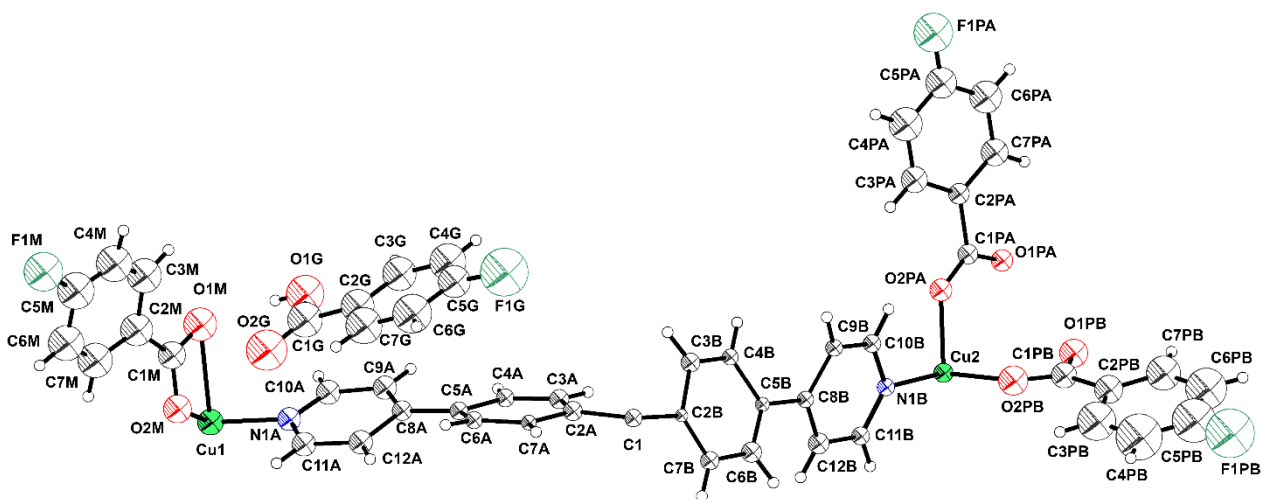


Figure S19: Ortep view of the asymmetric unit of TPPM-mCPW(*p*-FPh) (probability level 30%).

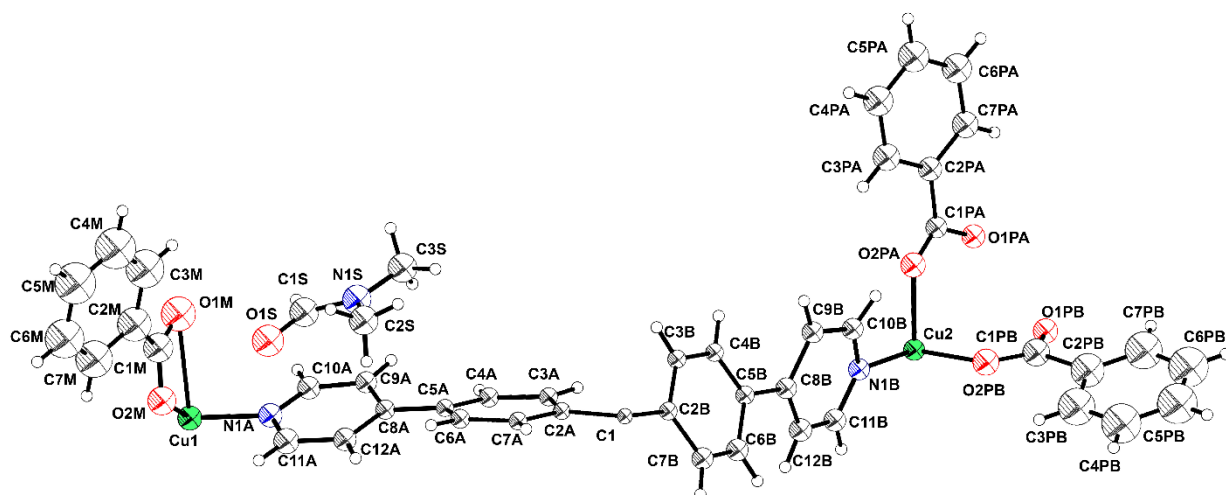


Figure S20: Ortep view of the asymmetric unit of TPPM-mCPW(Ph) (probability level 30%).

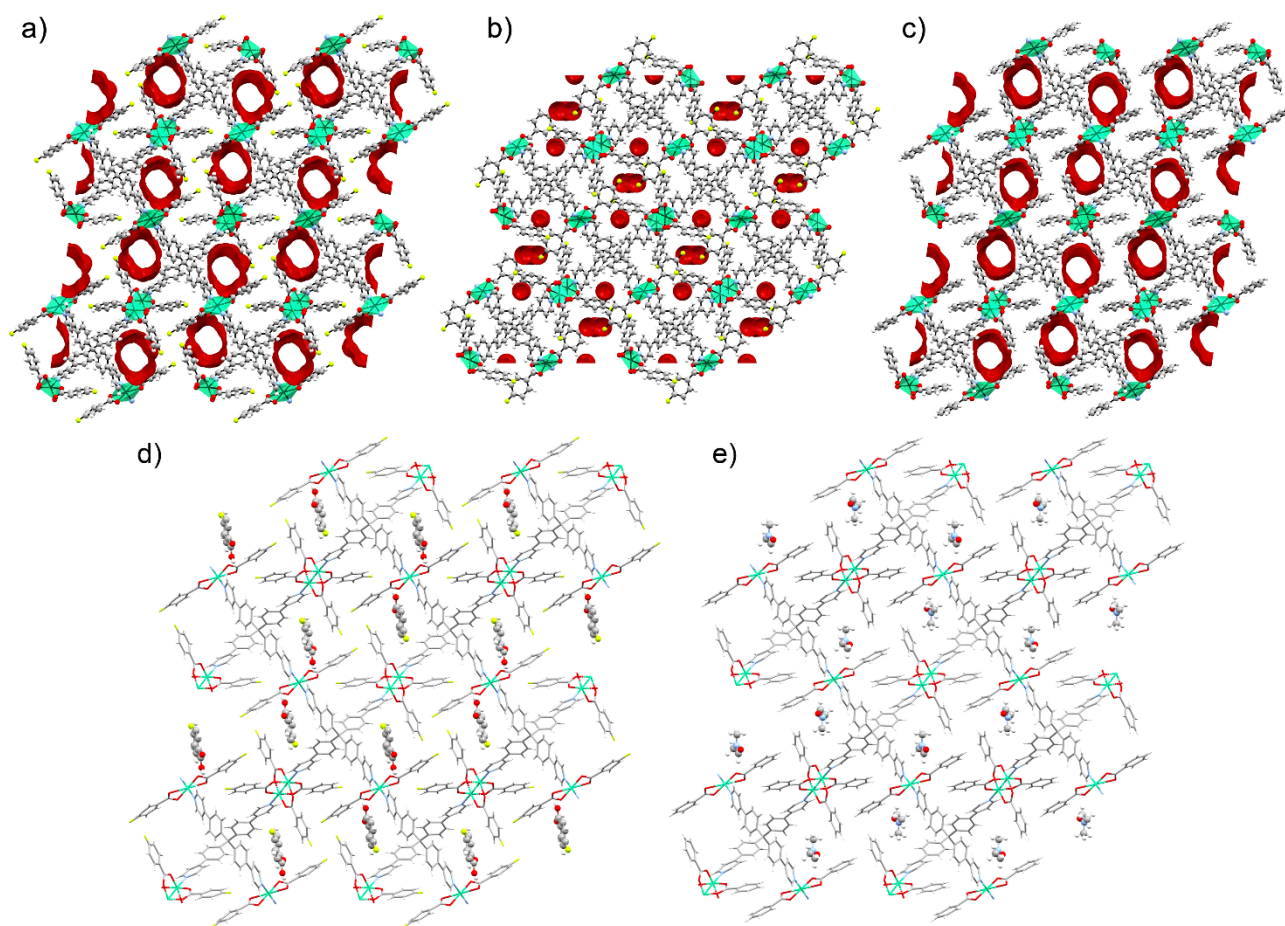


Figure S21: Crystal structure of: *op*-TPPM-mCPW(*p*-FPh) (a, d), *cp*-TPPM-mCPW(*p*-FPh) (b) and *op*-TPPM-mCPW(Ph) (c, e). The open pore (op) structures have been represented with surfaces that highlight their channels (a, c) and with the guest molecules that were experimentally modelled (d, e). Each structure is oriented along its crystallographic *b*-axis with its relative voids as an orange surface. The theoretical voids have been calculated by removing eventual guest molecules and using a probe radius of 1.2 Å.

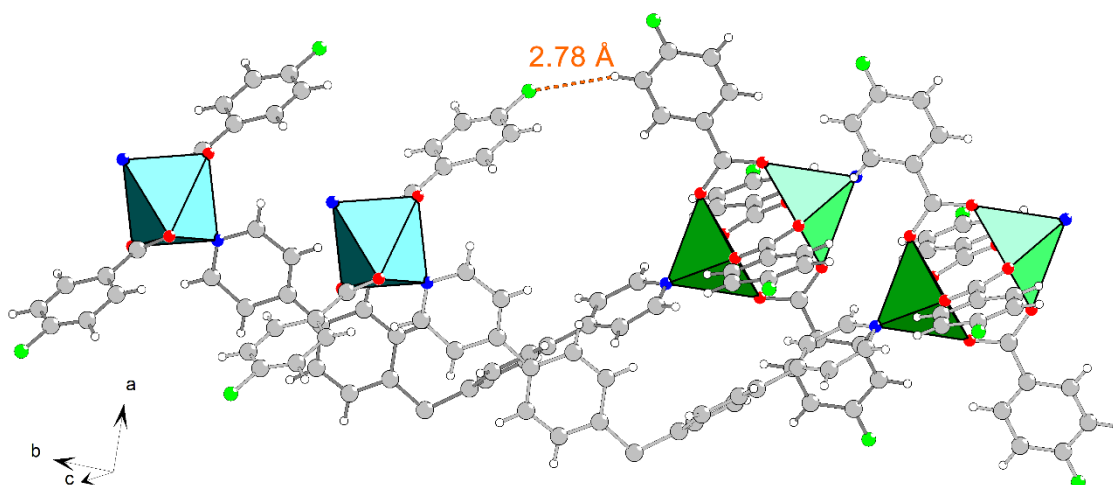


Figure S22: CH...F contacts between two interwoven nets in the *op*-TPPM-mCPW(*p*-FPh) crystal structure.

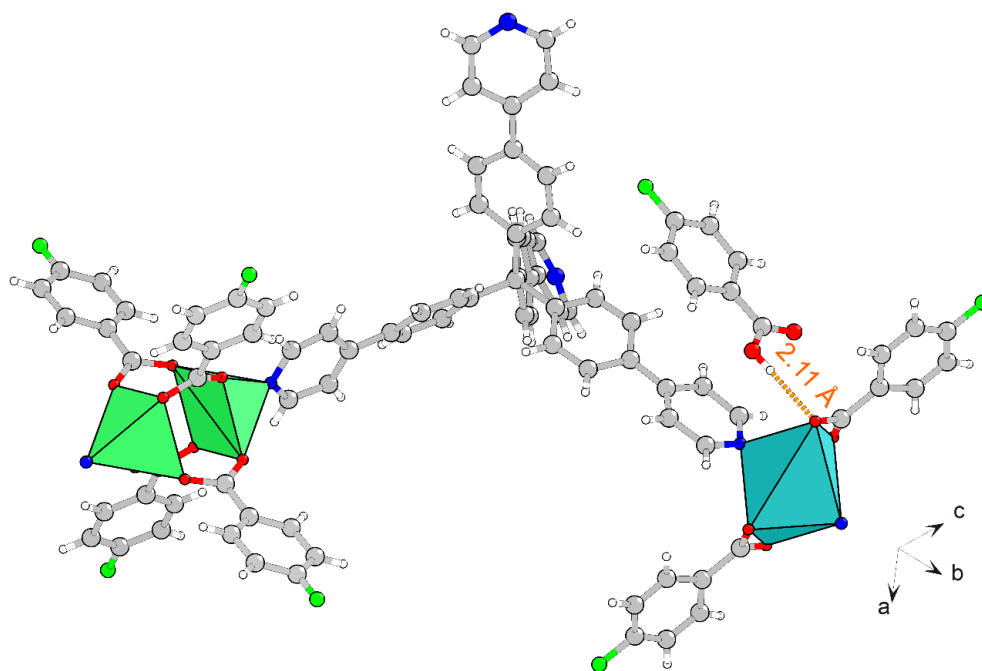


Figure S23: Hydrogen bond interaction between the guest *p*-FPhA molecule and the framework in *op*-TPPM-mCPW(*p*-FPh) crystal structure.

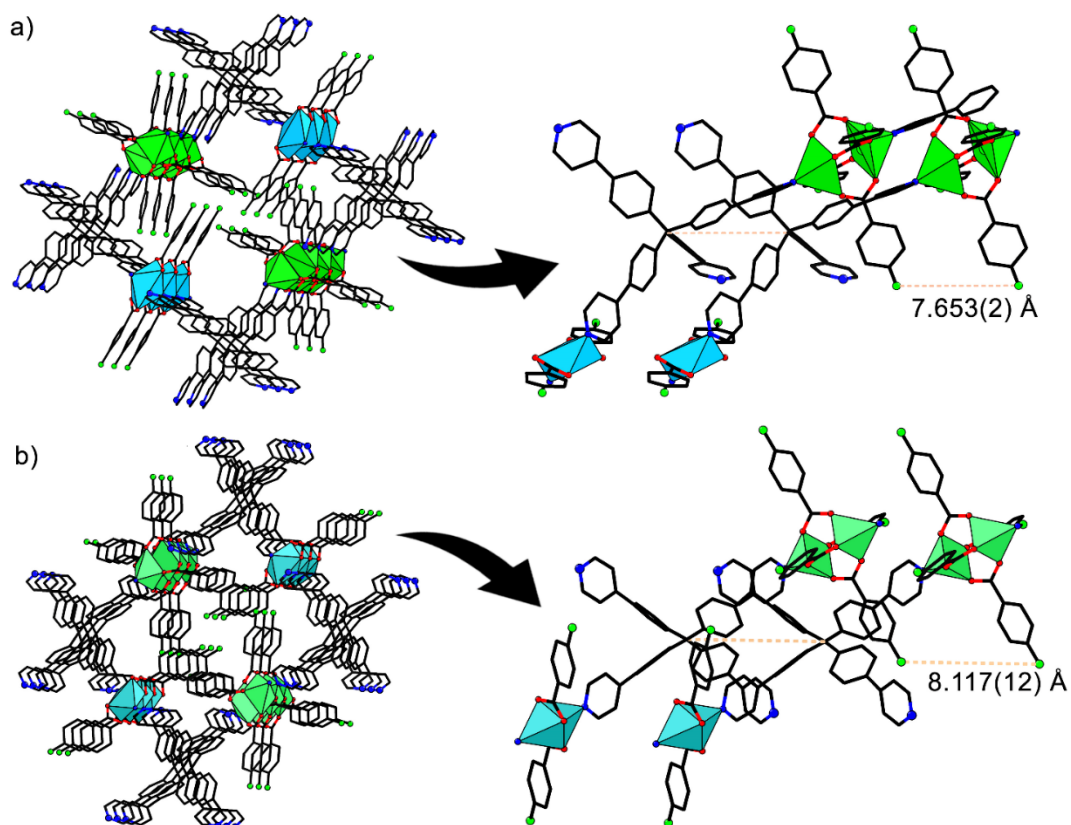


Figure S24: View of the inter-framework distances along the *b*-axis direction for (a) *op*-TPPM-mCPW(*p*-FPh) and (b) *cp*-TPPM-mCPW(*p*-FPh).

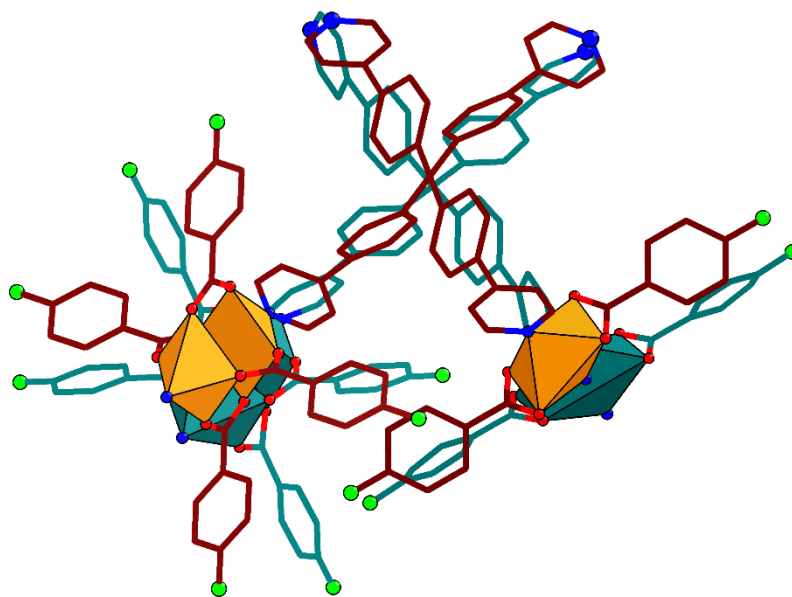


Figure S25: Overlay between the framework repeating units of *op*-TPPM-mCPW(*p*-FPh), in blue, and *cp*-TPPM-mCPW(*p*-FPh), in red.

5 Thermogravimetric Analyses (TGA)

The thermogravimetric analyses were conducted on a Perkin Elmer Instrument, model TGA 8000. The experiments were carried out in the temperature range 30-450°C with a heating rate of 20°C min⁻¹ under air flux.

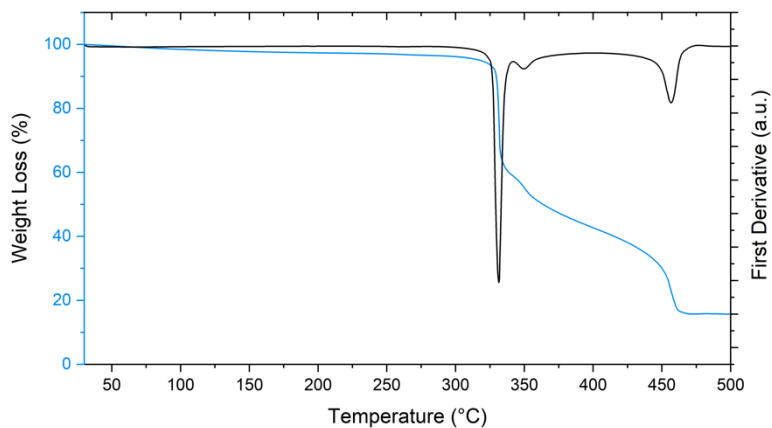


Figure S26: Thermogravimetric path recorded on the *cp*-TPPM-mCPW(*p*-FPh) crystal phase after the washing process.

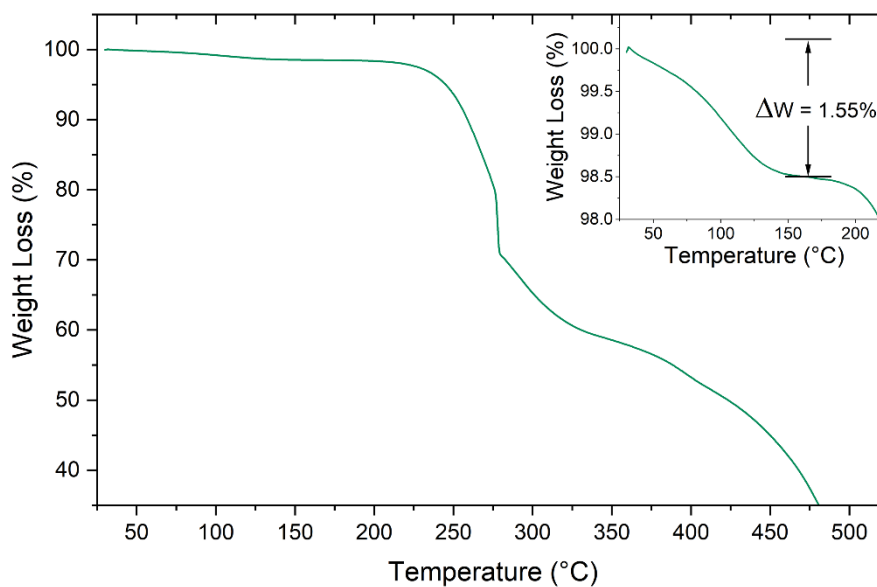


Figure S27: Thermogravimetric path recorded on the *op*-TPPM-mCPW(Ph) crystal phase.

6 PFAS adsorption experiments

The ^{19}F NMR analyses were recorded on a Jeol 600 MHz ECZ600R. The relaxation delay was regulated at 120 s and 64 scans have been collected for each sample.

6.1 MOF digestion

6.1.1 Sample preparation for ^{19}F NMR analysis

The ^{19}F NMR spectra were collected in 450 μL of $\text{DMSO-}d_6$ with 50 μL of $\text{DCI/D}_2\text{O}$ (2:8), to completely digest the material. This is essential to hamper the influence of the paramagnetic Cu(II) ions, which induce an overall peak broadening. Moreover, the **TPPM-mCPW(Ph)** spectra were recorded with the addition of 50 μL of 0.03 mM aqueous solution of trifluoroethanol (TFE) as internal standard.

6.1.2 PFAS exposure experiment

The adsorption experiments were carried out in triplicate for both **TPPM-mCPW(Ph)** and **TPPM-mCPW(*p*-FPh)** MOFs. The procedure consisted of placing about 1 mg of the MOF into a 1.5 mL Eppendorf vial, followed by the addition of 1 mL of a 5 mM solution of **NaPFB** or **NaPFO**. After 24 hours, the aqueous solution was removed by centrifugation, and the solid was rinsed two times with distilled water. Then, 50 μL of a 2:8 $\text{DCI/D}_2\text{O}$ solution were added to the solid to completely degrade its polymeric network. Subsequently, the product was completely solubilized in $\text{DMSO-}d_6$ and characterized through ^{19}F NMR spectroscopy.

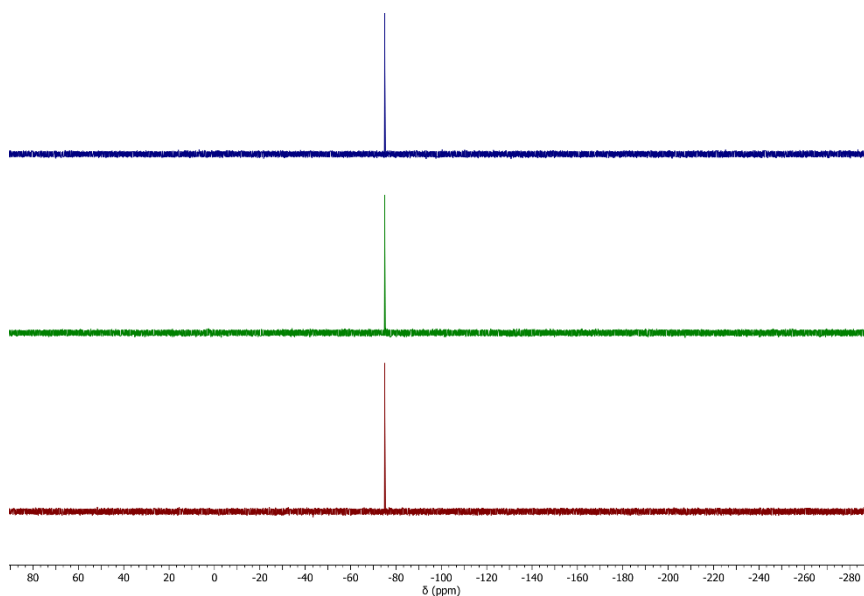


Figure S28: ^{19}F NMR spectra of **TPPM-mCPW(Ph)** after the exposure to the **NaPFB** solution. (565 MHz, $\text{DMSO-}d_6$) δ (ppm): -75.8 (t, $J = 8.8$ Hz, 3F, TFE). In the recorded spectra, no signals of **NaPFB** were observed; only the internal standard peak was detected.

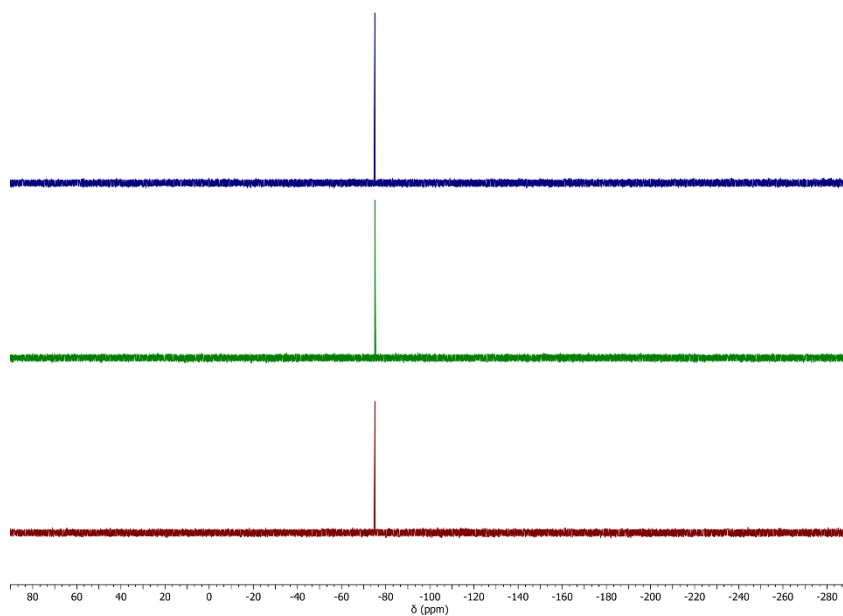


Figure S29: ^{19}F NMR spectra of TPPM-mCPW(Ph) after the exposure to the NaPFO solution. (565 MHz, DMSO- d_6) δ (ppm): -75.8 (t, $J = 8.8$ Hz, 3F, TFE). In the recorded spectra, no signals of NaPFO were observed; only the internal standard peak was detected.

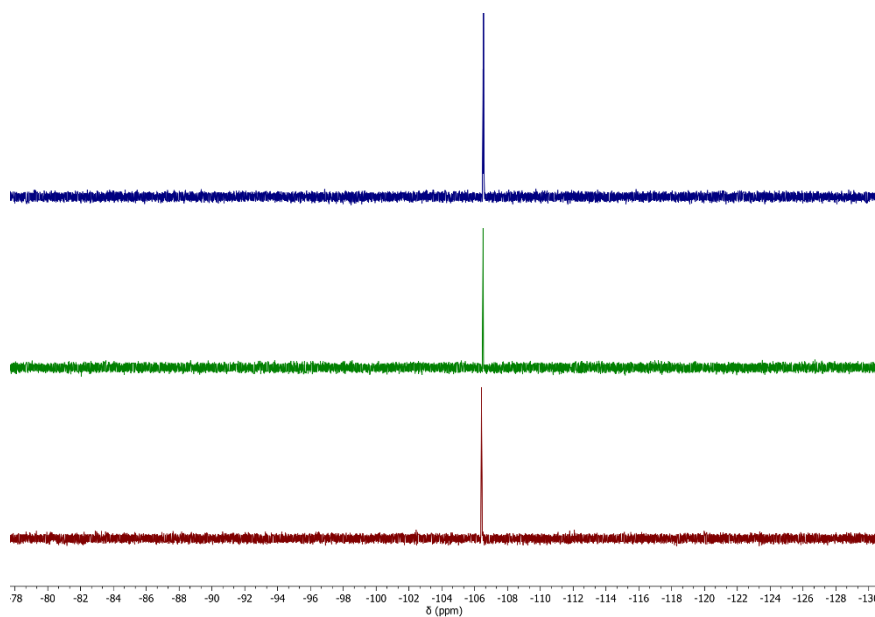


Figure S30: ^{19}F NMR spectra of TPPM-mCPW(*p*-FPh) after the exposure to the NaPFB solution. (565 MHz, DMSO- d_6) δ (ppm): -106.5 (m, 6F, *p*-FPhA). In the recorded spectra, no signals of NaPFB were observed; only the *p*-FPhA peak from the framework was detected.

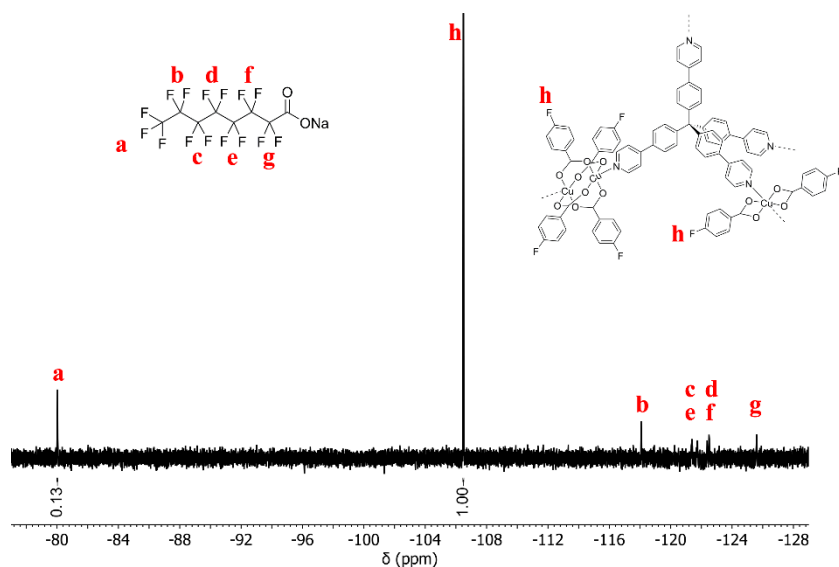


Figure S31: ^{19}F NMR spectrum of TPPM-mCPW(*p*-FPh) after the exposure to the NaPFO solution, first experiment. (565 MHz, $\text{DMSO-}d_6$) δ (ppm): -80.4 (t, $J = 9.70$ Hz, 3F, a), -106.5 (m, 6F, h), -118.1 (m, 2F, b), -121.4 (m, 2F, c), -121.7 (m, 2F, d), -122.4 (m, 2F, e), -122.5 (m, 2F, f), -125.6 (m, 2F, g).

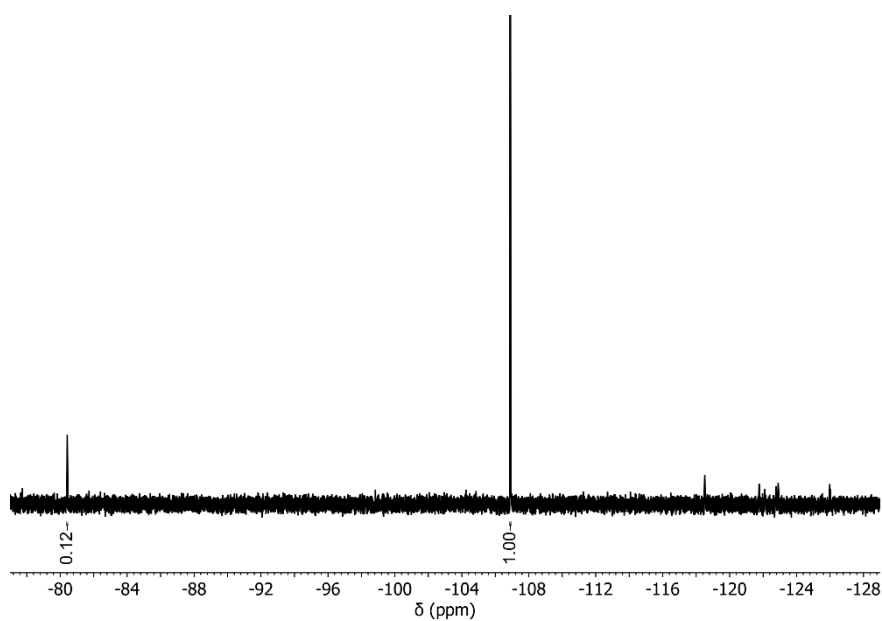


Figure S32: ^{19}F NMR spectrum of TPPM-mCPW(*p*-FPh) after the exposure to the NaPFO solution, second experiment.

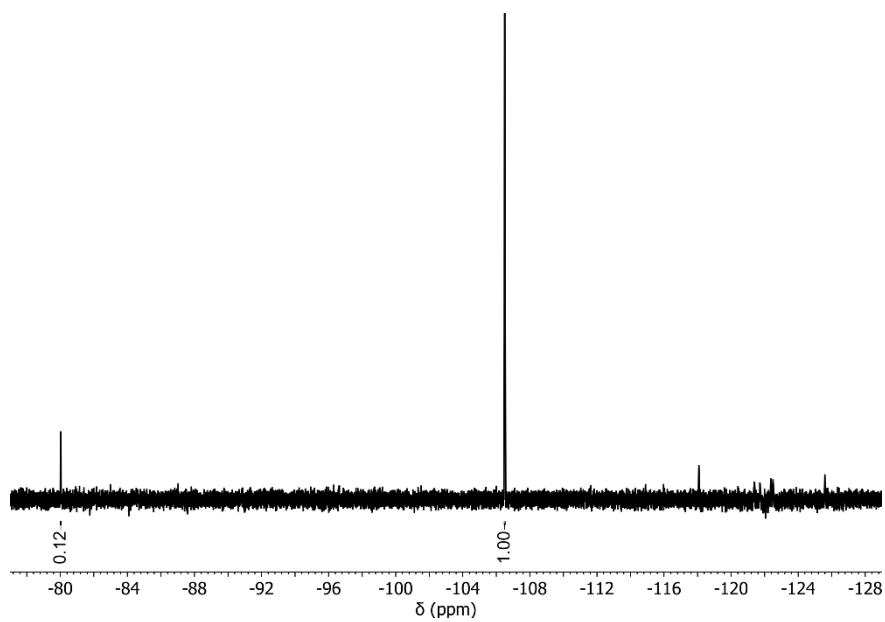


Figure S33: ¹⁹F NMR spectrum of TPPM-mCPW(*p*-FPh) after the exposure to the NaPFO solution, third experiment.

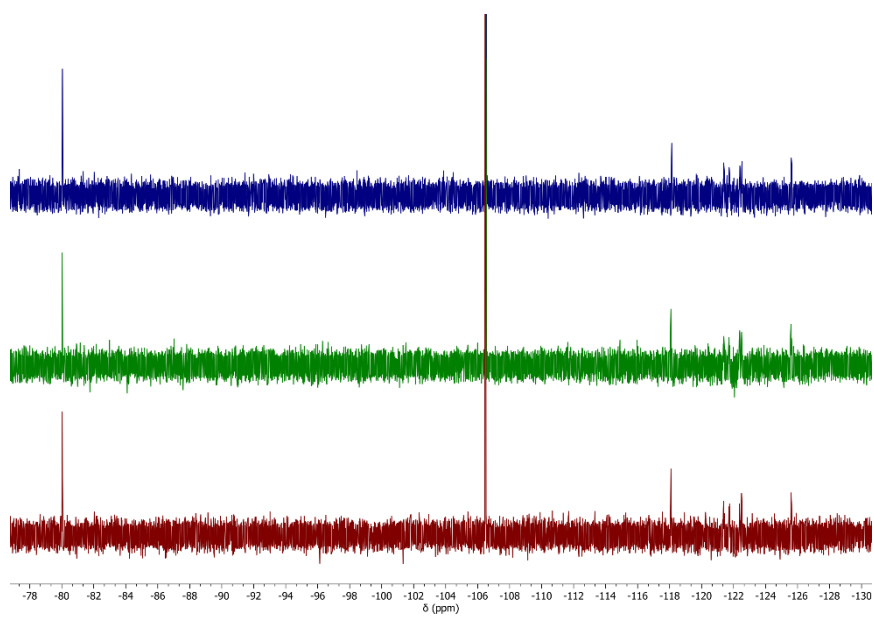


Figure S34: ¹⁹F NMR spectra of TPPM-mCPW(*p*-FPh) after the exposure to the NaPFO solution, stacked view of the three experiments.

6.2 Uptake of NaPFO using TPPM-mCPW(*p*-FPh) from aqueous solution

The adsorption experiments were conducted at different concentrations of NaPFO (C_0) to evaluate the maximum adsorption capacity (q_{\max}) and the adsorption equilibrium constant (K) of TPPM-mCPW(*p*-FPh). The *op*-TPPM-mCPW(*p*-FPh) MOF (~ 1 g/L) was suspended in deionised water through sonication (~ 20 min). Different amounts of NaPFO stock solutions were added to the MOF suspensions and stirred for 2 hours at room temperature. Subsequently, after centrifugation, 0.5 mL of each solution was transferred into an NMR-tube along with 0.5 mL of a TFE solution as internal standard (2.3 mM for C_0 equal and above 150 mg/L and 0.57 mM for C_0 below 150 mg/L) in 8:2 H₂O/D₂O. The NaPFO uptake was evaluated through integration of the NMR signals corresponding to the CF₃ groups of TFE (I_{TFE}) and perfluorooctanoate ($I_{\text{CF}_3\text{-PFO}}$).

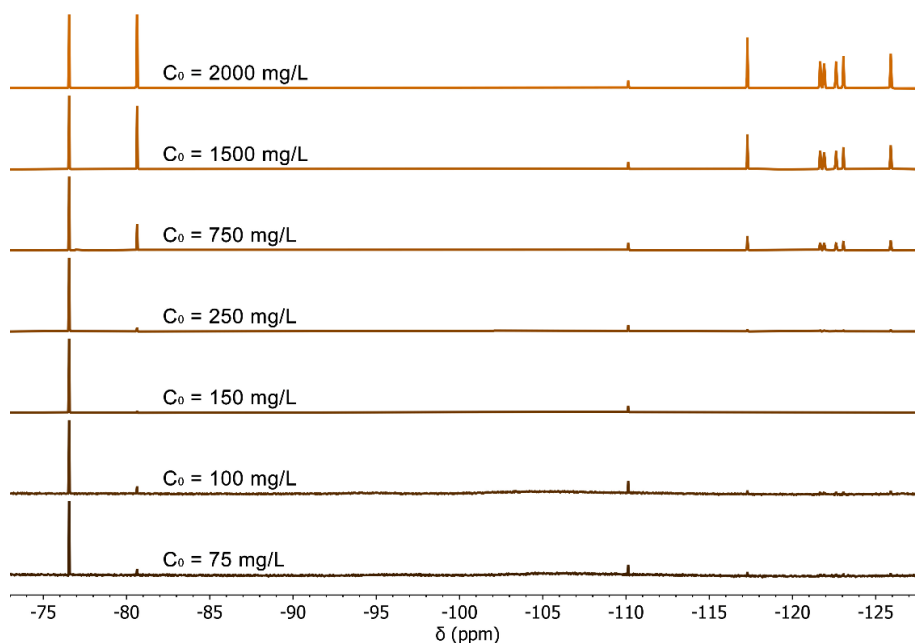


Figure S35: ¹⁹F NMR spectra of the NaPFO solution after the exposure experiment to the suspension of *op*-TPPM-mCPW(*p*-FPh).

Table S7: Calculated NaPFO uptake from ¹⁹F NMR spectroscopy.

C_0 (mg/L)	I_{TFE}	$I_{\text{CF}_3\text{-PFO}}$	NaPFO uptake (mg/g)
75 ^a	100	8.52	54.2
100 ^a	100	12.0	70.6
150 ^b	100	1.99	128
250 ^b	100	5.17	195
750 ^b	100	46.5	256
1500 ^b	100	114	291
2000 ^b	100	162	284
1000 ^b	100	94.1	0 (Blank)
100 ^a	100	40.9	0 (Blank)

[a] 0.57 mM TFE solution as internal standard; [b] 2.3 mM TFE solution as internal standard.

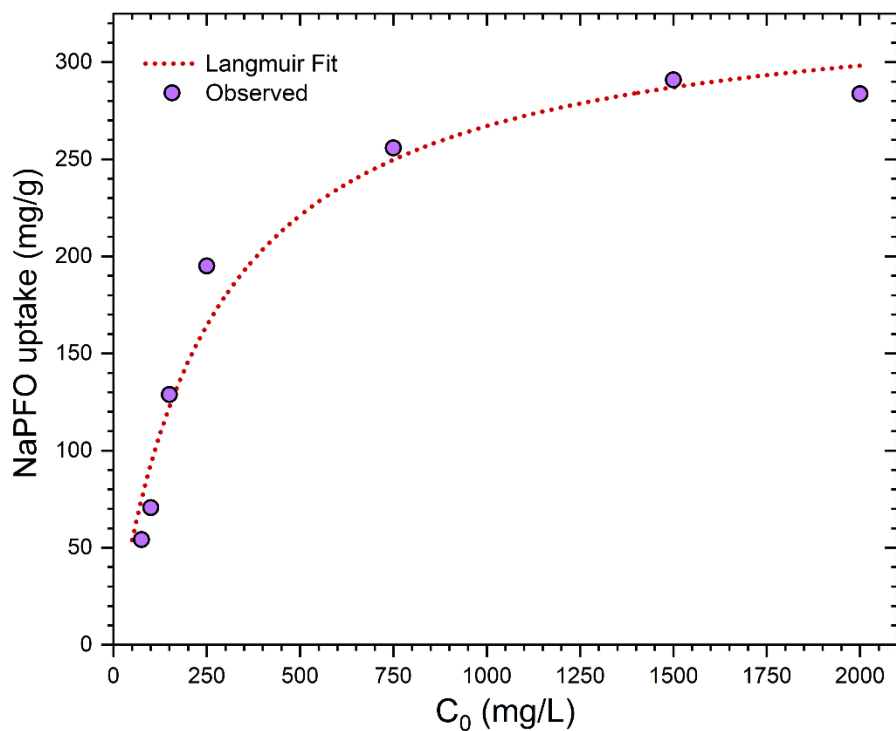


Figure S36: NaPFO uptake and relative Langmuir fitting for *cp*-TPPM-mCPW(*p*-FPh).

The NaPFO uptake at the equilibrium was fitted according to the Langmuir equation:

$$q = q_{\max} \cdot \frac{K \cdot C}{1 + K \cdot C}$$

Table S8: Parameters of the calculated Langmuir isotherm.

Parameters	<i>cp</i> -TPPM-mCPW(<i>p</i> -FPh)
q_{\max} (mg/g)	336 ± 21
K (L/mg)	$(3.9 \pm 0.8) \cdot 10^{-3}$
R^2	0.96

7 DLS Measurement

The DLS analysis on solvothermal and mechanochemical *cp*-TPPM-mCPE(*p*-FPh) MOFs was conducted on a Malvern Zetasizer Nano ZSP. The sample was prepared by dispersing 2 mg of MOF in 10 mL of microfiltered deionised water followed by 20 minutes of sonication. Then 500 μ L of the suspension were diluted with 9.5 mL of microfiltered deionised water and 1 mL of this solution was transferred into a quartz cuvette.

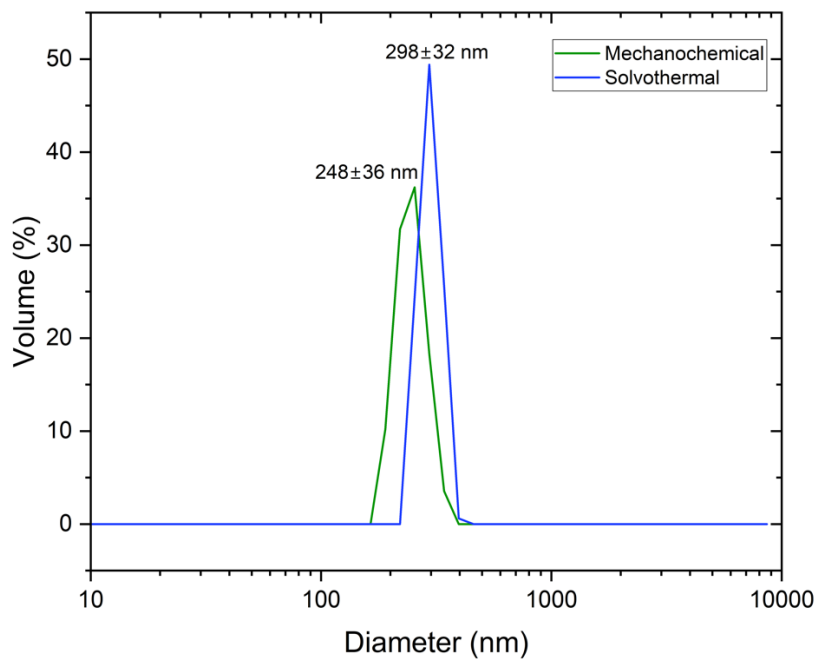


Figure S37: DLS analysis carried out on the solvothermal and mechanochemical *cp*-TPPM-mCPE(*p*-FPh) MOFs.

8 Computational Studies

The electrostatic potential running along the framework channels of *op*-TPPM-mCPW(Ph) and *op*-TPPM-mCPW(*p*-FPh) was calculated using the Materials Studio software suite.¹⁴ The calculation was carried out with the D3Mol package with a GGA-PBE functional, considering the crystal symmetry and unrestricted spin. The calculated potential was subsequently displayed in Figure 4 over the electron density map (isovalue 0.2).

The theoretical void calculations reported in the main text were conducted with Mercury4 software¹⁵ using a hydrogen probe. Instead, the geometric properties of the frameworks of *op*-TPPM-mCPW(Ph), *op*-TPPM-mCPW(*p*-FPh) and *cp*-TPPM-mCPW(*p*-FPh) were calculated using the PoreBlazer v4.0 software.¹⁶ The calculation was conducted using a helium probe and the results are reported in Table S9.

Table S9: Geometric properties of TPPM-mCPW MOFs calculated using PoreBlazer v4.0.

	<i>op</i> -TPPM-mCPW(Ph)	<i>op</i> -TPPM-mCPW(<i>p</i> -FPh)	<i>cp</i> -TPPM-mCPW(<i>p</i> -FPh)
System Volume (Å ³)	4209.23	4478.71	4095.64
Maximum Pore Diameter (Å)	4.82	4.82	2.97
Network-accessible Surface Area (m ² g ⁻¹)	109.32	128.51	0
Network-accessible Volume (Å ³)	757.43	827.30	277.76

The molecular geometry optimization of perfluorobutanoate (PFB) and perfluorooctanoate (PFO) was conducted using Gaussian16 software suite.¹⁷ For ground-state geometrical optimisations, was used a DFT theory level with a B3LYP functional, a 6-31+(d,p) basis set and a CPCM solvation model (water). The volume of the geometrically optimised molecules was calculated through the MoloVol v1.2 software package (Figure S38).¹⁸ The calculated molecular volumes (Table S10) and network-accessible volume (Table S9) were then employed for the estimation of the theoretical maximum uptake of PFONa (q_{max}^{teo}). The molecular volume of NaPFO was defined by combining the volume of PFO, reported in Table S10, with the van der Waals volume of Na,¹⁹ accordingly with the following equation:

$$q_{max}^{teo} = \frac{V_{MOF}^{void}}{V_{NaPFO} \cdot Z} \cdot \frac{MW_{NaPFO}}{MW_{MOF}} \cdot 10^3 = 352.22 \text{ mg/g}$$

where V_{MOF}^{void} (Å³) is the *op*-TPPM-mCPW(*p*-FPh) networks-accessible volume, V_{NaPFO} (Å³) is the NaPFO molecular volume, Z is the number of chemical formula units contained in the unit cell, MW (g/mol) the molar mass while 10^3 is a conversion factor.

Table S10: Molecular volumes and sizes calculated from the geometrically optimised PFB and PFO fragments.

	<i>PFB</i>	<i>PFO</i>
Van der Waals Volume (\AA^3)	123.48	228.27
Molecular Volume (\AA^3)	131.01	244.16
Minimum Size – a (\AA)	4.3	4.6
Maximum Size – b (\AA)	8.3	4.6

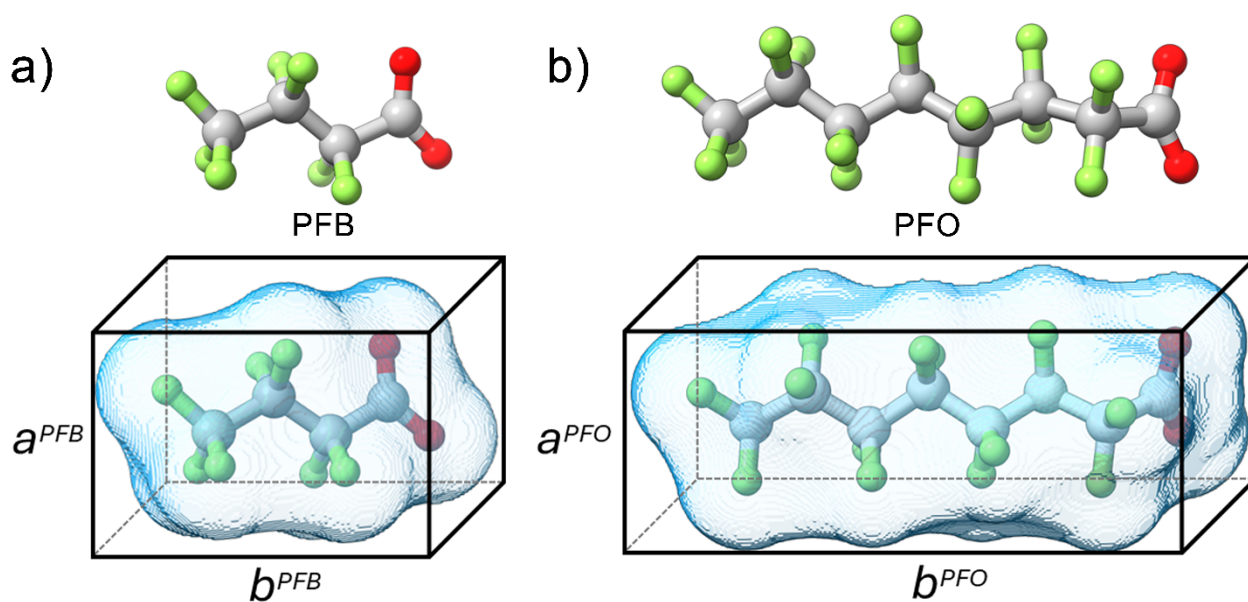


Figure S38: Perfluorobutanoate (PFB) and perfluorooctanoate (PFO) molecules (a, b) after geometrical optimisation calculations. The blue surface highlights the calculated molecular volume region: $V^{PFB} = 131.0 \text{ \AA}^3$; $V^{PFO} = 244.2 \text{ \AA}^3$. The axis dimensions of the box surrounding the molecules correspond to their average size and were calculated based on the cross-sectional values of their volume surface: $a^{PFB} \approx 4.3 \text{ \AA}$, $b^{PFB} \approx 8.3 \text{ \AA}$; $a^{PFO} \approx 4.6 \text{ \AA}$, $b^{PFO} \approx 12.6 \text{ \AA}$.

9 References

- 1 D. Marchetti, N. Riboni, A. K. Inge, O. Cheung, M. Gemmi, E. Dalcanale, F. Bianchi, C. Massera and A. Pedrini, *Chem. Mater.*, 2025, **37**, 2230–2240.
- 2 H. Kitagawa, H. Ohtsu and M. Kawano, *Angew. Chem. Int. Ed.*, 2013, **52**, 12395–12399.
- 3 D. Marchetti, F. Portone, F. Mezzadri, E. Dalcanale, M. Gemmi, A. Pedrini and C. Massera, *Chemistry A European J*, DOI:10.1002/chem.202202977.
- 4 G. M. Sheldrick, SADABS v2.03: Area-Detector Absorption Correction. 1999.
- 5 G. M. Sheldrick, *Acta Crystallogr A Found Adv*, 2015, **71**, 3–8.
- 6 G. M. Sheldrick, *Acta Crystallogr C Struct Chem*, 2015, **71**, 3–8.
- 7 O. V. Dolomanov, L. J. Bourhis, R. J. Gildea, J. A. K. Howard and H. Puschmann, *J Appl Crystallogr*, 2009, **42**, 339–341.
- 8 V. Petříček, M. Dušek and L. Palatinus, *Zeitschrift für Kristallographie - Crystalline Materials*, 2014, **229**, 345–352.
- 9 A. A. Coelho, *J Appl Crystallogr*, 2018, **51**, 210–218.
- 10 D. Marchetti, N. Riboni, A. K. Inge, O. Cheung, M. Gemmi, E. Dalcanale, F. Bianchi, C. Massera and A. Pedrini, *Chemistry of Materials*.
- 11 F. Bertocchi, D. Marchetti, S. Doria, M. Di Donato, C. Sissa, M. Gemmi, E. Dalcanale, R. Pinalli and A. Lapini, *Chemistry A European J*, 2023, e202302619.
- 12 L. Palatinus, P. Brázda, M. Jelínek, J. Hrdá, G. Steciuk and M. Klementová, *Acta Crystallogr B Struct Sci Cryst Eng Mater*, 2019, **75**, 512–522.
- 13 L. Palatinus and G. Chapuis, *J Appl Crystallogr*, 2007, **40**, 786–790.
- 14 M. Meunier and S. Robertson, *Molecular Simulation*, 2021, **47**, 537–539.
- 15 C. F. Macrae, I. Sovago, S. J. Cottrell, P. T. A. Galek, P. McCabe, E. Pidcock, M. Platings, G. P. Shields, J. S. Stevens, M. Towler and P. A. Wood, *J Appl Crystallogr*, 2020, **53**, 226–235.
- 16 L. Sarkisov, R. Bueno-Perez, M. Sutharson and D. Fairen-Jimenez, *Chem. Mater.*, 2020, **32**, 9849–9867.
- 17 Gaussian 09, Revision D.01, Frisch, M. J.; Trucks, G. W.; Schlegel, H. B.; Scuseria, G. E.; Robb, M. A.; Cheeseman, J. R.; Scalmani, G.; Barone, V.; Petersson, G. A.; Nakatsuji, H.; Li, X.; Caricato, M.; Marenich, M.; Bloino, J.; Janesko, B. G.; Gomperts, R.; Mennucci, B.; Hratchian, H. P.; Ortiz, J. V.; Izmaylov, A. F.; Sonnenberg, J. L.; Williams-Young, D.; Ding, F.; Lipparini, F.; Egidi, F.; Goings, J.; Peng, B.; Petrone, A.; Henderson, T.; Ranasinghe, D.; Zakrzewski, V. G.; Gao, J.; Rega, N.; Zheng, G.; Liang, W.; Hada, M.; Ehara, M.; Toyota, K.; Fukuda, R.; Hasegawa, J.; Ishida, M.; Nakajima, T.; Honda, Y.; Kitao, O.; Nakai, H.; Vreven, T.; Throssell, K.; Montgomery, J. A.; Peralta, Jr., J. E.; Ogliaro, F.; Bearpark, M.; Heyd, J. J.; Brothers, E.; Kudin, K. N.; Staroverov, V. N.; Keith, T.; Kobayashi, R.; Normand, J.; Raghavachari, K.; Rendell, A.; Burant, J. C.; Iyengar, S. S.; Tomasi, J.; Cossi, M.; Millam, J. M.; Klene, M.; Adamo, C.; Cammi, R.; Ochterski, J. W.; Martin, R. L.; Morokuma, K.; Farkas, O.; Foresman, J. B., Fox, D. J. Gaussian, Inc., Wallingford CT, 2016.
- 18 J. B. Maglic and R. Lavendomme, *J Appl Crystallogr*, 2022, **55**, 1033–1044.
- 19 S. Alvarez, *Dalton Trans.*, 2013, **42**, 8617.